SHAPED HOLE EFFECTS ON FILM COOLING EFFECTIVENESS AND A COMPARISON OF MULTIPLE EFFECTIVENESS MEASUREMENT TECHNIQUES

A Thesis

by

TRENT ALAN VARVEL

Submitted to the Office of Graduate Studies of
Texas A&M University
in partial fulfillment of the requirements for the degree of

MASTER OF SCIENCE

December 2004

Major Subject: Mechanical Engineering

SHAPED HOLE EFFECTS ON FILM COOLING EFFECTIVENESS AND A COMPARISON OF MULTIPLE EFFECTIVENESS MEASUREMENT TECHNIQUES

A Thesis

by

TRENT ALAN VARVEL

Submitted to the Office of Graduate Studies of
Texas A&M University
in partial fulfillment of the requirements for the degree of

MASTER OF SCIENCE

Approved as to style and content by:

Je-Chin Han (Chair of Committee)	Warren Heffington (Committee)
Hamn-Ching Chen (Committee)	Dennis O'Neal (Head of Department)

December 2004

Major Subject: Mechanical Engineering

ABSTRACT

Shaped Hole Effects on Film Cooling Effectiveness and a

Comparison of Multiple Effectiveness Measurement Techniques. (December 2004)

Trent Alan Varvel, B.S., Texas A&M University

Chair of Advisory Committee: Dr. Je-Chin Han

This experimental study consists of two parts. For the first part, the film cooling effectiveness for a single row of seven cylindrical holes with a compound angle is measured on a flat surface using five different measurement techniques: steady-state liquid crystal thermography, transient liquid crystal thermography, pressure sensitive paint (PSP), thermocouples, and infrared thermography. A comparison of the film cooling effectiveness from each of the measurement techniques is presented. All methods show a good comparison, especially for the higher blowing ratios. The PSP technique shows the most accurate measurements and has more advantages for measuring film cooling effectiveness. Also, the effect of blowing ratio on the film cooling effectiveness is investigated for each of the measurement techniques.

The second part of the study investigates the effect of hole geometries on the film cooling effectiveness using pressure sensitive paint. Nitrogen is injected as the coolant air so that the oxygen concentration levels can be obtained for the test surface. The film effectiveness is then obtained by the mass transfer analogy. Five total hole geometries are tested: fan-shaped laidback with a compound angle, fan-shaped laidback with a simple angle, a conical configuration with a compound angle, a conical configuration with a simple angle, and the reference geometry (cylindrical holes) used in part one. The effect of blowing ratio on film cooling effectiveness is presented for each hole geometry. The spanwise averaged effectiveness for each geometry is also presented to compare the geometry effect on film cooling effectiveness. The geometry of the holes has little effect

on the effectiveness at low blowing ratios. The laterally expanded holes show improved effectiveness at higher blowing ratios.

All experiments are performed in a low speed wind tunnel with a mainstream velocity of 34 m/s. The coolant air is injected through the coolant holes at four different coolant-to-mainstream velocity ratios: 0.3, 0.6, 1.2, and 1.8.

DEDICATION

To my wife, parents, and brothers for their endless love, support, and encouragement.

ACKNOWLEDGEMENTS

I am very grateful to Dr. Je-Chin Han for mentoring me throughout my career here at Texas A&M University. He has provided me with invaluable experience as a research assistant and insight into the gas turbine industry. I would also like to thank Dr. Warren Heffington and Dr. Hamn-Ching Chen for serving on my committee and offering valuable suggestions to improve my research and reports. My appreciation and thanks goes out to all of my research partners in the lab who offered experienced wisdom during my time in the graduate program. I would also like to acknowledge Siemens Westinghouse Power Corporation, who provided funding for this study.

TABLE OF CONTENTS

Page

ABSTRACT iii
DEDICATION v
ACKNOWLEDGEMENTS vi
TABLE OF CONTENTS vii
LIST OF FIGURES ix
LIST OF TABLES xiii
NOMENCLATURE xiv
INTRODUCTION AND LITERATURE REVIEW 1
Injection Hole Shape 3
Effects of Blowing Rates 5
Arrays for Shaped Holes 6
Leading Edge Shaped Holes 8
Free-Stream Turbulence Effects 9
Effect of Tabs on Film Cooling Holes 12
Discharge Coefficients for Shaped Holes 13
OBJECTIVES 16
MEASUREMENT THEORY 17
Liquid Crystal Thermograhpy 18
Steady State Technique 18
Transient Technique 18
Pressure Sensitive Paint Technique 20
Thermocouples 22
Infrared Thermography 22
INSTRUMENTATION 24
RESULTS AND DISCUSSION 32
Part 1: Comparison of Effectiveness Measurement Techniques 32
Steady State Liquid Crystal Thermography 32
Transient Liquid Crystal Thermography 38
PSP 44
Thermocouples 49
Infrared Thermography 51
Overall Comparison 57

Page

Part 2: Comparison of Hole Geometries 63
Plate 1 63
Plate 2 66
Plate 3 69
Plate 4 71
Plate 5 74
Overall Comparison 77
CONCLUSIONS 81
REFERENCES 83
VITA 88

LIST OF FIGURES

Page

Figure 1. Blade cooling techniques 2
Figure 2. Three temperature model for film cooling effectiveness 17
Figure 3. 3-D model of wind tunnel 25
Figure 4. Experimental setup for steady-state liquid crystal, transient liquid crystal, and PSP measurement techniques 26
Figure 5. Experimental setup for thermocouple and IR measurement techniques 27
Figure 6. Overview of film cooling hole geometries: a) cylindrical with compound angle, b) conical with compound angle, c) laid-back fan-shaped with compound angle, d) conical with axial angle, and e) laid-back fan-shaped with axial angle 29
Figure 7. Smooth test surface piece used for the liquid crystal and PSP techniques 30
Figure 8. Test surface piece used for the thermocouple and IR techniques 31
Figure 9. Calibration curve for the 20ºC bandwidth liquid crystal 33
Figure 10. Local effectiveness plots of Plate 1 using the steady state liquid crystal method for blowing ratios of (a) 0.3, (b) 0.6, (c) 1.2, and (d) 1.8 34
Figure 11. (a) Laterally averaged effectiveness of Plate 1 using the steady state liquid crystal method, (b) area of the 3 middle holes of Plate 1 used to average the effectiveness 36
Figure 12. Laterally averaged effectiveness of Plate 1 using the steady state liquid crystal method plotted versus x/D 37
Figure 13. Temperature model of test section showing the conduction effect on effectiveness measurements 38
Figure 14. Calibration curve of the two bandwidths used for the transient liquid crystal method 39
Figure 15. Local effectiveness plots of Plate 1 using the transient liquid crystal method for blowing ratios of (a) 0.3, (b) 0.6, (c) 1.2, and (d) 1.8 41

Page

Figure 16. (a) Laterally averaged effectiveness of Plate 1 using the transient liquid crystal method, (b) area of the 3 middle holes of Plate 1 used to average the effectiveness....42
Figure 17. Laterally averaged effectiveness of Plate 1 using the transient liquid crystal method versus the x/D parameter....43
Figure 18. Calibration curve used for the PSP method....45
Figure 19. Local effectiveness plots of Plate 1 using the PSP method for blowing ratios of (a) 0.3, (b) 0.6, (c) 1.2, and (d) 1.8....46
Figure 20. (a) Laterally averaged effectiveness of Plate 1 using the PSP method, (b) area of the 3 middle holes of Plate 1 used to average the effectiveness....47
Figure 21. Laterally averaged effectiveness versus the x/D parameter of Plate 1 using the PSP method....48
Figure 22. (a) Laterally averaged effectiveness of Plate 1 using the thermocouple method, (b) area of the 3 middle holes of Plate 1 used to average the effectiveness....50
Figure 23. Laterally averaged effectiveness versus the x/D parameter of Plate 1 using the thermocouple method....51
Figure 24. Calibration curve of the IR camera system....53
Figure 25. Local effectiveness plots of Plate 1 using the IR method for blowing ratios of (a) 0.3, (b) 0.6, (c) 1.2, and (d) 1.8....54
Figure 26. (a) Laterally averaged effectiveness of Plate 1 using the IR method, (b) area of the 3 middle holes of Plate 1 used to average the effectiveness....55
Figure 27. Laterally averaged effectiveness of Plate 1 using the IR method plotted versus x/D....56
Figure 28. Effectiveness comparison of all measurement methods for Plate 1....58

Page

Figure 29. Effectiveness comparison of all measurement methods for Plate 1 plotted versus the x/D parameter 59
Figure 30. Laterally averaged effectiveness of M = 0.6 measured by the PSP method compared with that measured from other sources. 60
Figure 31. Laterally averaged effectiveness of M = 1.2 measured by the PSP method compared with that measured from other sources. 61
Figure 32. Laterally average effectiveness results for Plate 1 with and without the turbulence grid taken by the IR system 62
Figure 33. Local effectiveness plots of Plate 1 using PSP for blowing ratios of (a) 0.3, (b) 0.6, (c) 1.2, and (d) 1.8 64
Figure 34. Laterally averaged effectiveness for the three middle holes of Plate 1 plotted versus the x/D parameter 65
Figure 35. Laterally averaged effectiveness for the three middle holes of Plate 1 plotted versus the x/MS parameter 65
Figure 36. Local effectiveness plots of Plate 2 using PSP for blowing ratios of (a) 0.3, (b) 0.6, (c) 1.2, and (d) 1.8 66
Figure 37. Laterally averaged effectiveness for the three middle holes of Plate 2 plotted versus the x/D parameter 68
Figure 38. Laterally averaged effectiveness for the three middle holes of Plate 2 plotted versus the x/MS parameter 68
Figure 39. Local effectiveness plots of Plate 3 using PSP for blowing ratios of (a) 0.3, (b) 0.6, (c) 1.2, and (d) 1.8 69
Figure 40. Laterally averaged effectiveness for the three middle holes of Plate 3 plotted versus the x/D parameter 70
Figure 41. Laterally averaged effectiveness for the three middle holes of Plate 3 plotted versus the x/MS parameter 71

Page

Figure 42. Local effectiveness plots of Plate 4 using PSP for blowing ratios of (a) 0.3, (b) 0.6, (c) 1.2, and (d) 1.8 72
Figure 43. Laterally averaged effectiveness for the three middle holes of Plate 4 plotted versus the x/D parameter 73
Figure 44. Laterally averaged effectiveness for the three middle holes of Plate 4 plotted versus the x/MS parameter 73
Figure 45. Local effectiveness plots of Plate 5 using PSP for blowing ratios of (a) 0.3, (b) 0.6, (c) 1.2, and (d) 1.8 74
Figure 46. Laterally averaged effectiveness for the three middle holes of Plate 5 plotted versus the x/D parameter 75
Figure 47. Laterally averaged effectiveness for the three middle holes of Plate 5 plotted versus the x/MS parameter 76
Figure 48. Comparison of the PSP and Thermocouple laterally averaged effectiveness measurements for the three middle holes of Plate 5 77
Figure 49. Effectiveness comparison of Plates 1 - 5 plotted versus the x/D parameter 78
Figure 50. Effectiveness comparison of Plates 1 - 5 plotted versus the x/MS parameter 79

LIST OF TABLES

Page

Table 1. Test parameters from Cho et al. [8] 4
Table 2. Summary of shaped hole geometries. 28

NOMENCLATURE

AR	area ratio
c_p	specific heat of test section
C_{mix}	oxygen concentration of mainstream-coolant mixture
C_∞	oxygen concentration of mainstream
D	inlet hole diameter
h	local heat transfer coefficient ($W / m^2 K$)
k	thermal conductivity of test surface (0.1812 W / mK)
L	hole length
M	blowing ratio
q''	local convective heat flux (W / m^2)
S	equivalent slot width (total inlet hole area / total pitch)
T_{aw}	local adiabatic wall temperature (°C)
T_c	coolant temperature (°C)
T_m	mainstream temperature (°C)
T_w	local surface temperature (°C)
Tu	turbulence intensity
V_c	coolant velocity (m / s)
V_m	mainstream velocity (m / s)
x	distance downstream of holes
α	thermal diffusivity of test section (1.073 x 10^{-7} m^2/s)

β lateral injection angle

θ streamwise injection angle

ν kinematic viscosity of air ($1.5534 * 10^{-5}\ m^2 / s$)

ρ density of air at 20º C ($1.1766\ kg / m^3$)

η film cooling effectiveness parameter

INTRODUCTION AND LITERATURE REVIEW

The gas turbine industry is always seeking to raise the thermal efficiency of the gas turbine engine by increasing the turbine inlet temperature. Increasing the operating temperature, however, leads to some major problems. Turbine blades, for example, are not able to withstand such high temperatures and thermal stresses. The design operating temperature in a gas turbine far surpasses the melting temperature of most materials. In modern gas turbines, sophisticated cooling schemes are implemented to help protect the blades and vanes from thermal failure. Numerous cooling techniques are described in Han et al. [1]. Cooling methods used to remove heat from the inside of the blade include impingement cooling, rib-turbulated cooling, and pin-fin cooling. Figure 1 depicts the typical cooling methods of modern gas turbine blades. Film cooling is an external cooling technique in which cool air is bled from the compressor stage, ducted to the internal chambers of the turbine blades, and discharged through small holes in the blade walls into the hot mainstream. This air provides a thin, cool, insulating blanket along the external surface of the turbine blade. As a result, the blade is able to sustain higher operating temperatures and achieve higher life cycles.

This thesis follows the style of ASME Journal of Turbomachinery.

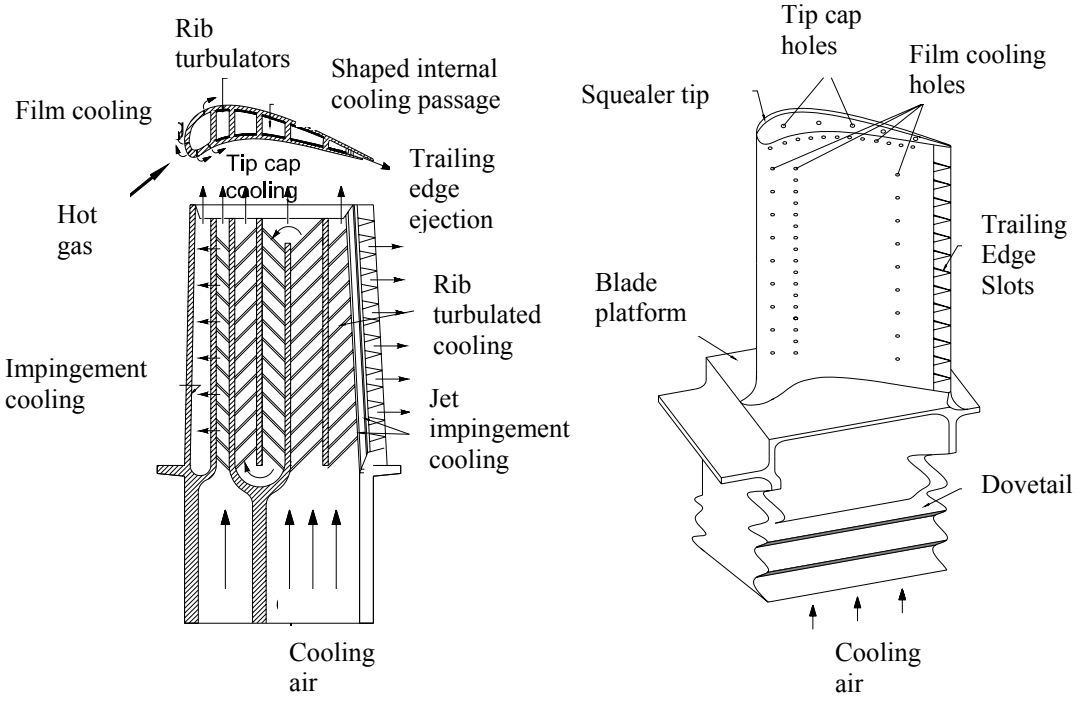

Figure 1. Blade cooling techniques

To increase gas turbine efficiencies, designers and researchers are trying to achieve the maximum cooling performance from the least amount of coolant air possible. It has recently been discovered that the injection hole geometry has a significant effect on the cooling efficiency. Thanks to new machining and manufacturing techniques such as laser drilling and electric-discharge machining, complex injection hole shapes are possible.

Shaped holes are currently being studied to help improve film cooling. Two major problems associated with film cooling are as follows: (1) the injected coolant usually penetrates into the mainstream resulting in a loss of the protective coolant layer, and (2) the region between the discrete injection holes is not covered well by the coolant. As a result, hot spots are formed on the blade surface because of the non-uniform distribution of the film coolant in the lateral direction.

Several solutions to increase film cooling performance have been studied extensively. For example, higher and more uniform film cooling is achieved with compound angle injection configurations. Compound angle holes reduce the axial momentum of the coolant and enhance the lateral momentum. Shaped holes provide better film cooling because of their expanded exit hole area. The widened area reduces the momentum of the high velocity coolant jet which spreads the coolant more laterally.

The efficiency of film cooling is quantified by a parameter known as film cooling effectiveness, η. It is defined in Equation 1, where T_f is the film temperature, T_m is the mainstream temperature, and T_c is the coolant temperature.

$$\eta = \frac{T_f - T_m}{T_c - T_m} \tag{1}$$

Injection Hole Shape

Many experimental studies have investigated the injection hole geometry effects on film cooling effectiveness. Goldstein et al. [2] were the first to research the use of shaped injection holes to improve film cooling performance. They tested a 10º spanwise-diffused hole and found that the shaped hole provided better film cooling characteristics than the common cylindrical hole. The shaped hole reduced the coolant momentum of the jet which prevented the coolant from lifting off of the surface. As a result, the coolant had less penetration into the mainstream when compared to the cylindrical holes, and the film cooling performance was enhanced.

In addition to laterally diffused holes, Sen et al. [3] and Schmidt et al. [4] studied forward diffused holes. They discovered that the 15º forward diffused holes also exhibit better effectiveness than cylindrical holes. Thole et al. [5] measured the flow fields for three types of injection holes: a cylindrical hole, a laterally diffused hole, and a forward-

laterally diffused hole. Their results showed that diffusing the injection hole reduces the coolant penetration into the mainstream and reduces the intense shear regions when compared to cylindrical holes.

Hyams and Leylek [6] and Brittingham and Leylek [7] performed numerical studies on shaped holes with streamwise and compound injections. They showed that vortices downstream of the cylindrical holes are unfavorable to film cooling performance. Shaped holes, on the other hand, can control the strength and size of the vortices to help enhance the film cooling performance.

In 2001, Cho et al. [8] studied the film effectiveness and heat transfer for three hole geometries with compound angles using the naphthalene sublimation technique. This method allowed the researchers to calculated local data for the regions around the holes. Shaped hole #1 diffuses 4º in all directions, while shaped hole #2 has a forward diffusion of 8º. The streamwise injection angle (θ) for all holes is 30º. The test section is set up so that the lateral injection angle (β) can be set to 0º, 45º, and 90º. Table 1 summarizes the parameters for each of the hole shapes.

Table 1. Test parameters from Cho et al. [8]

Hole geometry	D [mm]	AR	L/D	θ	β	M	DR
Cylindrical hole	20	1.00	5.0	30º	0º	1.0	1.0
Shaped hole # 1	13	2.55	4.0		45º	0.5, 1.0, 2.0	
Shaped hole # 2	13	2.48	5.4		90º	1.0	

The cylindrical hole has a very narrow region of high effectiveness because the jet penetrates into the mainstream. The compound angle ($\beta > 0º$), however, improves the coverage of the cylindrical hole due to the enhancement of lateral momentum. As a result, the high effectiveness region becomes wider. The effectiveness for shaped hole #1 showed that the coolant jet attaches well to the surface and has a broad coverage due

to the lateral diffusion of the hole. The effectiveness is much higher than the cylindrical hole and has a more uniform coverage.

Therefore, Cho et al. [8] concluded that the jet stream in the passage of shaped hole #1 is filled and diffused effectively with the expansion angle of 4º. Like the cylindrical hole, the high effectiveness region of shaped hole #1 extends further downstream with the increasing lateral injection angle of the hole.

Shaped hole #2 shows a narrower region of high effectiveness when compared to shaped hole #1. This is because the coolant on the upstream side of the hole is separated from the surface, and as a result, the coolant jet becomes less diffused with separation. The film cooling effectiveness is lower than that of shaped hole #1. Like the cylindrical and shaped hole #1, the compound injection angle of shaped hole #2 also increases the region of high effectiveness.

Effects of Blowing Rates

Effects of blowing rates for the coolant air have been extensively studied to determine how to achieve the optimum film cooling effectiveness. Optimizing the blowing rate is critical because blowing rates that are too high lose more coolant into the mainstream, where as low blowing rates do not provide enough coolant to effectively cover the surface. Studies have also shown the optimum blowing rates are not the same for every hole shape.

Goldstein et al. [2, 9] and Jubran and Brown [10] all showed general conclusions that the optimum blowing ratio for cylindrical holes is around M = 0.5. The higher blowing rates lowered the effectiveness as the coolant jets penetrated into the mainstream. Further downstream the effectiveness tended to increase with the blowing rate where the coolant jets reattached to the surface.

Cho et al. [8] compared the blowing rate effects for different hole shapes. The data for the lateral injection angle of $\beta = 45^{o}$ was used for comparison. With the cylindrical hole, a wide effectiveness region was observed for the low blowing rate because the coolant was attached to the surface. However, as the blowing rate increased, the coolant became more separated from the surface, and effectiveness decreased even with the compound angle. The optimum blowing rate for cylindrical holes is close to M = 0.5 for this study. Shaped hole #1 also showed decreasing effectiveness for increasing blowing rates. However, high effectiveness values were maintained for blowing rates up to M = 1.0. Shaped hole #2 exhibited similar patterns when compared to the other holes. At the highest blowing rate of M = 2.0, the effectiveness distribution was more similar to the cylindrical hole rather than the shaped hole #1. Because this hole has an expansion in the forward direction only, the diffusion of coolant in the hole is not uniform. Therefore the interaction between the mainstream and the coolant is stronger.

Arrays for Shaped Holes

Many studies of shaped hole film cooling effectiveness use only a single row of holes. The effectiveness of the single row of holes decreases when compared to that of a continuous slot due to the three-dimensional flow field downstream of the injection. Several researchers have focused on injection from a double row of cylindrical holes in order to approach a two-dimensional film cooling situation. Jubran and Brown [10], Jabbari et al. [11], and Jubran and Maiteh [12] have all shown that for the same injected mass flow rate per unit span, the double row provides better cooling protection than the single row. The increased area ratio of the double row lowers the momentum of the coolant which provides better lateral spreading of the coolant. Spacing the holes closer together also increases the effectiveness in the lateral direction. Ligrani et al. [13] showed that a compound angle orientation of the holes in the second row also increases the effectiveness. In addition, staggered rows of holes show better performance than inline rows of holes.

Dittmar et al. [14] studied the effectiveness of two simple hole geometries arranged as staggered double row and two shaped hole geometries arranged in a single row using an infrared camera system. Even though the blowing rates for the first two configurations are different from the last three, the same amount of total injected coolant mass flow per unit span is the same. Overall, the shaped holes showed the best effectiveness. Another important result was shown when the coolant flow was injected into the holes from the opposite direction of the angled holes. This "bent" coolant flow showed a much lower effectiveness than when the coolant air was injected into the holes from the same direction of the angled holes — a "direct" coolant injection. If the cooling air is fed from the opposing direction of the angled holes, the inflow into the hole is disturbed. As a result, the coolant does not follow the contour of the hole, and that leads to a decrease of surface protection.

Even with the double row, the cylindrical configurations show a lower effectiveness that the single row of shaped holes for all blowing rates because they allow more coolant to penetrate into the mainstream. The coolant is not as uniform as the shaped holes, especially in the near-hole region. Also, due to high momentum in the double row of cylindrical holes, the first row of holes creates a blockage effect on the second row. A wake region behind the injection carries the hot mainstream directly to the wall. This is caused by a complex vortex generation in the shear layer between the coolant jet and mainstream. The double row of slots seems to counter this vortex generation problem by deflecting the coolant jet closer to the surface because it matches the performance of the shaped holes further downstream because the stretching of the holes creates a wider geometrical coverage. The shaped holes still show a little higher effectiveness than the double row cylindrical holes due to the increased lateral spreading of the coolant.

At the higher blowing rate, the shaped holes clearly show improved effectiveness by minimizing the coolant separation from the surface. The jet separation can be improved by using slots instead of holes. The effectiveness is still somewhat lower than that of the

shaped holes, but the higher momentum is well transported downstream. Therefore the decay of effectiveness for the slots is not as strong as that of the shaped holes.

Leading Edge Shaped Holes

Most studies of film cooling effectiveness for shaped holes have been performed with flat plates. They have not considered the curvature effects seen in a real turbine blade, especially on the leading edge of a blade. Kim and Kim [15] tested five different injection hole configurations for the leading edge using an infrared camera. The leading edge of a blade is simulated by a cylinder.

It was shown that for low blowing rates, the trajectory of the first row of holes merged into the exit of the second row. The trajectory of the second row was nearly aligned with the mainstream direction. As the blowing rate increases, though, the trajectory of the second row deviates from the centerline of the holes. It was also noted that the pressure difference across the first row of holes was smaller than that across the second row due to the pressure distribution around the cylinder surface.

The film cooling effectiveness is slightly improved with the shaped holes. Walters and Leylek [16] found a low momentum region along the downstream edge of the cooling hole and a high momentum region on the upstream side of the hole. The shaped holes helped increase the low momentum region near the hole exit.

For the lowest blowing rate of M = 0.7, Kim and Kim [15] showed that a low effectiveness between the first row of holes existed near the stagnation region. Because the first row of holes has low momentum, lateral spreading of the coolant is weak. The shaped holes exhibited the highest effectiveness. For M = 1.3, all shaped holes provide uniform distributions of coolant at the stagnation region. The low effectiveness regions of Shapes C and E are reduce, but Shapes B and D show the highest effectiveness due to

strong lateral momentum. Finally for M = 1.7, all shaped holes show better effectiveness than the cylindrical holes. Once again, the laid-back fan-shaped hole shows the highest effectiveness, and the effectiveness for laid-back shaped hole decreased by 6% from the M = 1.3 case. This suggests that laid-back hole is more influenced by increasing the blowing rate, as compared with other shaped holes, due to the coolant separation.

For leading edge shaped holes, it was determined by Kim and Kim [15] that the blowing rate has a very strong effect on effectiveness and coolant trajectory. The cylindrical holes had increasing separation from the surface as the blowing rate increased. The laid-back holes showed the highest effectiveness with wider and more inclined trajectory at the hole centerline. However, the laid-back fan-shaped holes showed relatively low effectiveness because the additional streamwise expansion created insufficient lateral momentum. Overall, the laid-back fan-shaped hole provides the best effectiveness, and its effect remains further downstream.

Free-Stream Turbulence Effects

Turbulence intensity levels from the exit of the combustor can range anywhere from 7 to 20%. As a result, the turbulence inlet boundary condition for a first stage vane can be as high as 20%. According to Saumweber et al. [17], as the air is accelerated through the vane, the free-stream turbulence intensity will be reduced due to strong acceleration inside of the vane passage. Free-stream turbulence levels at engine conditions can therefore be in the range of 8 to 12%.

A majority of the studies performed on shaped hole film cooling have been tested at low free-stream turbulent intensities. Several recent studies have focused more on higher turbulent intensity levels. For cylindrical holes inclined 33º to the mainstream, Kadotani and Goldstein [18, 19] tested turbulent intensities ranging form 0.3 to 20.6% with length

scales between 0.06 and 0.33 hole diameters. At low blowing rates, high turbulent intensities produced a decrease in centerline effectiveness. At high blowing rates, however, high turbulence increased the centerline effectiveness. This was because the turbulent mixing reduced the penetration of the coolant into the mainstream. Additionally, the high turbulence improved the lateral distribution of the coolant for the cylindrical holes. Low turbulence, however, creates a more uniform lateral distribution of effectiveness.

Jumper et al. [20] studied turbulence ranging from 14 to 17% on cylindrical holes inclined 30º to the mainstream. They found that high turbulence reduced the effectiveness as well as the effective cooling length. In addition, high turbulence increased the optimum blowing rate. Bons et al. [21] showed that centerline effectiveness for cylindrical holes angled 35º to the mainstream decreased by 70% at turbulence as high as 17.4%. Between the holes, though, the effectiveness increased 50-100% with high free-stream turbulence.

An important finding by Burd et al. [22] was that the L/D ratio of the film cooling hole has to be taken into account when comparing turbulent intensity effects on film cooling. They performed hot wire anemometer measurements on cylindrical holes angled 35º to the mainstream at two turbulent intensities (0.5 and 12%) while varying the L/D ratio from 2.3 to 7. With low free-stream turbulence and short holes, the coolant is ejected farther from the wall and spreads more in the spanwise direction when compared to a long hole. At high free-stream turbulence, though, the flow differences between a long and short hole greatly decrease.

Because of these findings, Saumweber et al. [17] were the first to publish data concerning shaped holes at elevated free-stream turbulences. The three holes were cylindrical, fan-shaped, and laid-back fan-shaped. Using an infrared camera system, the researchers tested three film cooling hole shapes at turbulence intensities ranging from

3.6 to 11%. The blowing rates ranged from 0.5 to 2.5. The effectiveness for the fan-shaped holes responds differently to free-stream turbulence than that of the cylindrical holes. The effectiveness for shaped holes is reduced for all blowing rates as the turbulent intensity is increased. The cylindrical holes, though, show an increase in effectiveness at high blowing rates when the free-stream turbulence is increased. Since the fan-shaped holes have no tendency separate the coolant from the surface (even at high blowing rates), there is no potential for the turbulence to improve the spreading of the coolant in the lateral direction. The laid-back fan-shaped holes are similar to the fan-shaped holes, but the overall effectiveness levels are lower. The authors also concluded that increasing the L/D ratio from 2.1 to 3.5 at a constant turbulent intensity of 5.1% did not show a pronounced effect on the effectiveness.

Teng et al. [23, 24] examined the effects of hole shapes on turbine-blade heat transfer and film cooling performance under steady and unsteady wake conditions. The effect of an unsteady wakes produced by upstream vane trailing edges has a strong effect on rotor blade surface heat-transfer coefficient distributions. By using rotating rods at the inlet of the five blade cascade to produce an unsteady wake, the researches were able to simulate turbulence intensities as high as 20% inside the wake. The time-mean-averaged turbulence intensity was about 10.4%. For the cases without the unsteady wake effect, or without the rotating rods in the mainstream flow, the time-mean-averaged turbulence was about 0.7%. Teng et al. [24] compared cylindrical, fan-shaped, and laidback fan-shaped holes for a single row of nine holes located on the suction side gill-hole region of a turbine blade. They concluded that the shaped holes provided a better film cooling effectiveness than the cylindrical holes for both steady flow and unsteady flow with the wake effects. In addition, the fan-shaped holes performed better than the laidback fan-shaped holes. The researchers also showed that as the blowing ratio increased from 0.6 to 1.2, the effectiveness of the cylindrical holes decreased while the effectiveness of the shaped holes increased. The unsteady wake tends to decrease film cooling effectiveness, except for the higher blowing ratio cases (M = 0.8 and 1.2) from x/D = 0 to 25 for fan-

shaped holes, where the film cooling effectiveness increases. Ou et al. [25] and Mehendale et al. [26] simulated unsteady wake conditions over a linear turbine-blade cascade with film cooling. They studied the effects of unsteady wake on a model turbine blade with multiple-row film cooling using air and CO_2 as coolants. They measured heat transfer coefficients and film cooling effectiveness at discrete locations using thin foil heating and multiple thermocouples. They concluded that heat transfer coefficients increase and film cooling effectiveness values decrease with an increase in unsteady wake strength.

Effect of Tabs on Film Cooling Holes

Many techniques have been applied to the film cooling technology in order to improve the effectiveness. For example, compound angles clearly exhibit higher film cooling effectiveness with enhanced lateral coverage. Another technique that has been studied is using tabs to cover certain areas of the film cooling hole. Ekkad et al. [27] has shown tabs to significantly enhance the effectiveness up to 200%. Tabs help generate a vorticity at the exit of the hole that counters the kidney-pair vortex of the coolant jets, which in turn, helps reduce coolant penetration into the mainstream. The authors found that the optimum placement of the tabs is at the upstream edge. However, these results were only based on injection perpendicular to the mainstream.

Nasir et al. [28] studied the effect of tabs on the upstream edge of angled holes using the transient liquid crystal technique. The tabs are oriented (1) parallel to the surface, (2) downwards at –45º, and (3) upward at 45º as seen in Figure 12. The tabs were made of cardboard and in the shape of an equilateral triangle with sides of 1.27 cm and a height of 1.1 cm. The tabs covered 33% of the centerline length of the hole.

The holes with no tabs showed the jets separating from the surface and then reattaching downstream, where the effectiveness increases. The upward tabs had a much higher

effectiveness than no tabs, and complete spanwise coverage is achieved within two hole diameters. The downward tabs were very similar to the upward tabs, but the effectiveness values are slightly lower in the near hole region. Higher turbulence levels were observed for downward tabs, which might explain the lower effectiveness values due to more mixing of the mainstream. The upward tabs exhibit effectiveness even lower than the baseline case with no tabs. The authors concluded that the upward tabs enhance jet penetration into the mainstream because of the Coanda-type effect. The tabs deflect the mainstream around the holes, and this reduces the effect of the mainstream pushing the coolant jet downward to the surface.

The pressure drop was also considered in the study by Ekkad et al. [27]. The downward tabs showed the highest pressure drop, where as upward tabs showed no additional pressure drop across the hole.

Discharge Coefficients for Shaped Holes

Discharge coefficients are used to quantify the flow losses in the film cooling holes. Since the flow rate of the coolant is a key parameter in optimizing the cooling performance, the discharge coefficient is essential in designing an efficient cooling hole. Discharge coefficients have been proven to depend on many geometric and aerodynamic parameters like hole geometry and pressure ratios across the cooling hole. From the studies of Hay and Lampard [29], the main geometric parameters that discharge coefficients depend on are the following: hole inclination angle, hole orientation angle, hole length, and hole entry and exit radiusing. Because diffused holes are known to improve the cooling effectiveness, the authors studied discharge coefficients for these expansion holes. They found that the shaped holes increased the discharge coefficient when compared to cylindrical holes due to the pressure recovery in the expanded portion of the hole.

The effect of the mainstream flow on the discharge coefficients was studied by Hay et al. [30] as well as Rowbury et al [31]. The external mainstream flow is known to block the jet exiting hole which results in lower discharge coefficients when compared to no mainstream flow. Some configurations, though, have shown higher discharge coefficients do to the fact that the mainstream can effectively draw up the coolant jet flow.

Hay et al. [30] also investigated the effect of internal cross-flow on the discharge coefficient. The manner in which the coolant air is directed into the cooling holes can affect the cooling performance of the hole. As discussed earlier, Dittmar et al. [14] showed that the entry direction of the coolant into the hole can significantly affect the film cooling effectiveness. This is due to the change in discharge coefficient. Gritsch et al. [32] focused on the discharge coefficients of shaped holes with the internal cross-flow approaching perpendicular to the mainstream flow.

The same hole geometries of Saumweber et al. [17], were used by Gritsch et al. [32]: cylindrical hole, fan-shaped hole, and laid-back fan-shaped hole. They ran two sets of tests. In the first set, the coolant and mainstream were each run at a constant Mach numbers while the pressure ratio was varied from 1 to 2. In the second set of tests, the internal Mach number was varied from 0 to 0.6 for a given constant pressure ratio and no mainstream flow.

For the cylindrical holes, the mainstream Mach number effect depends on the internal Mach number. A reduction in static pressure at certain regions of the hole exit occur due to local acceleration of the mainstream flow. This increases the mass flow through the hole. The shaped holes showed similar trends to that of the cylindrical holes, but the effect of the mainstream Mach number is reduced even more, which is desirable. The shaped holes showed almost no mainstream Mach number effect because its expanded

exit area decreased the coolant momentum which in turn decreased the mainstream blockage effect.

Overall, the discharge coefficient values for the shaped holes are higher than the cylindrical holes. When no internal cross-flow is present, the discharge coefficients for the shaped holes are unaffected by the pressure ratio, which indicates that the flow through the holes is choked—even for low pressure ratios. The discharge coefficients for the additional lay-back hole are nearly the same as the regular fan-shaped hole.

It was also shown that the orientation of the internal cross-flow had an effect on the discharge coefficient. Gritsch et al. [32] ran tests with the internal cross-flow oriented perpendicular to the mainstream and parallel to the mainstream.

For the perpendicular orientation of the internal cross-flow, the discharge coefficient is decreased with increasing internal Mach number. For the parallel orientation, however, there is an internal Mach number for a given pressure ratio at which the discharge coefficient is at a maximum. Also for the perpendicular orientation, the discharge coefficients for the shaped holes are independent of mainstream Mach number; whereas for the cylindrical holes, the effect of the external Mach number is weak and depends on the pressure ratio and the internal Mach number.

OBJECTIVES

The objective of this study consist of two parts: (1) to compare the accuracy and precision of various film cooling effectiveness measuring techniques, and (2) to compare the geometry effects and blowing ratio effects of different hole shapes on the film cooling effectiveness. The results from these objectives will be presented as follows:

- Part 1 - detailed film cooling effectiveness results from the reference hole shape (Plate 1) will be presented for all of the measuring techniques for different coolant-to-mainstream velocity ratios (V_c / V_m = 0.3 ~ 1.8).

- Part 2 - detailed film cooling effectiveness results on various hole shapes (Plates 1 – 5) will be presented for different coolant-to-mainstream velocity ratios (V_c / V_m = 0.3 ~ 1.8). The film effectiveness will be measured using the pressure sensitive paint technique used in Part 1.

MEASUREMENT THEORY

There are several different methods used to calculate the film cooling effectiveness. These methods include liquid crystal thermography, pressure sensitive paint, thermocouples, and infrared thermography. An overview of the effectiveness measuring techniques is found in Han et al. [1]. Film cooling is a three temperature problem involving the mainstream temperature (T_m), the coolant temperature (T_c), and the wall temperature (T_w). Figure 2 shows a diagram for the three temperatures involved in film cooling. The following will describe in detail the theory behind each of these measurement techniques.

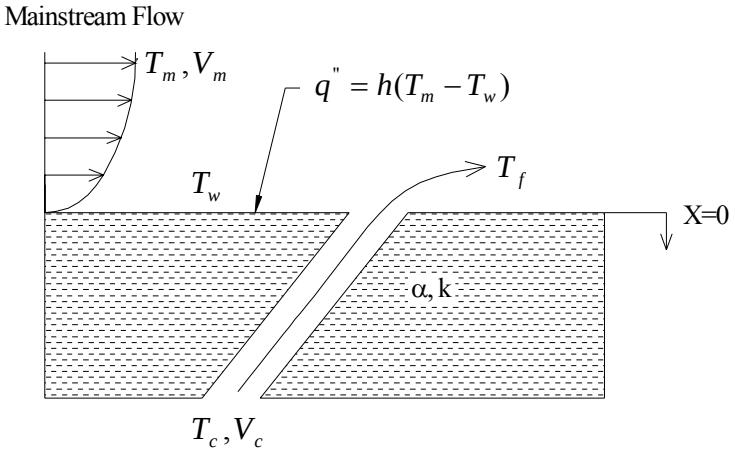

Figure 2. Three temperature model for film cooling effectiveness

Liquid Crystal Thermograhpy

Liquid crystals reflect different colors when exposed to temperature changes by reflecting a single wavelength of light. Different crystals reflect at different temperatures, but they can all be calibrated to particular temperatures. The two most common methods for measuring the film effectiveness include the steady-state technique and the transient technique.

Steady State Technique

The steady state technique, as described in Han et al. [1], records the color of the liquid crystals with a RGB camera. Every pixel in the data is then converted into a hue, saturation, and intensity. The local hue value can then be calibrated to a local temperature. It is important to note that the camera angle and lighting angles used during calibration must be identical to those used during the experiments. Any change in lighting or camera angles will cause the liquid crystals to reflect a different color. The test surface is made of low thermal conductivity so that the wall temperature is assumed to be adiabatic. The test section is exposed to the mainstream and coolant temperatures until steady-state conditions are reached. The RGB camera then records the surface temperature, which is assumed to be the adiabatic temperature. With the adiabatic wall temperature known (T_{aw}) Equation 2 can be used to find the effectiveness.

$$\eta = \frac{T_{aw} - T_m}{T_c - T_m} \tag{2}$$

Transient Technique

The transient liquid crystal technique is also used to measure the film cooling effectiveness, as described by Ekkad and Han [33] and Kwak and Han [34]. The local heat transfer coefficient over the liquid crystal coated surface can be obtained using Equation 3, the one dimensional semi-infinite solid assumption for the surface.

$$k\frac{\partial^2 T}{\partial x^2} = \rho c_p \frac{\partial T}{\partial t} \tag{3}$$

For the 1-D transient conduction equation, the initial conditions and the boundary conditions are seen in Equations 4 and 5:

$$at \quad t = 0, \quad T = T_i \tag{4}$$

$$at \quad x = 0, \quad -k\frac{\partial T}{\partial X} = h(T_w - T_m); \quad as \quad x \to \infty, \quad T = T_i \tag{5}$$

The solution to the above equation at the convective boundary surface (x=0) is seen in Equation 6:

$$\frac{T_w - T_i}{T_m - T_i} = 1 - \exp\left(\frac{h^2 \alpha t}{k^2}\right) erfc\left(\frac{h\sqrt{\alpha t}}{k}\right) \tag{6}$$

By knowing the initial temperature (T_i) of the surface, the mainstream temperature (T_m) in the wind tunnel, the color change wall temperature (T_w), and the color change time (t), the local heat transfer coefficient (h) can be calculated from Equation 6.

For film cooling over a flat surface, the mainstream temperature in Equation 6 is replaced by a film temperature (T_f), which is the temperature of the mixed mainstream and coolant. The film temperature, which controls the convection from the liquid crystal coated surface, is defined in terms of a non-dimensional temperature known as the film cooling effectiveness (η), defined in Equation 7.

$$\eta = \frac{T_f - T_m}{T_c - T_m} \quad or \quad T_f = \eta T_c + (1-\eta) T_m \tag{7}$$

Then Equations (6) and (7) are combined to yield Equation 8.

$$\frac{T_w - T_i}{T_f - T_i} = \frac{T_w - T_i}{\eta T_c + (1-\eta) T_m - T_i} = \left[1 - \exp\left(\frac{h^2 \alpha t}{k^2} \right) erfc\left(\frac{h\sqrt{\alpha t}}{k} \right) \right] \tag{8}$$

To obtain both the heat transfer coefficient and the film cooling effectiveness, it is necessary to obtain two equations to solve for the two unknowns (h and η).

Therefore, the transient technique requires two sets of tests to get the effectiveness and heat transfer coefficient at every pixel. The first test is run with both the mainstream and coolant at the ambient temperature. With the test section initially heated, the mainstream, coolant flow, and camera are simultaneously switched on. The time it takes for each pixel to reach a certain color (green due to its high intensity) is recorded. Since the coolant and mainstream temperatures are the same temperature, the film temperature can be assumed to be the same as the ambient mainstream temperature. Also, since the test surface has a low conductivity, it can be assumed a semi-infinite solid. Therefore, the heat transfer coefficient can then be found from Equation 8. A second identical test is run, except with the coolant temperature heated above the ambient mainstream temperature. The film effectiveness can then be solved from Equation 8 using the heat transfer coefficient obtained from the first test.

Pressure Sensitive Paint Technique

Pressure sensitive paint (PSP) is based on oxygen-quench photoluminescence. The intensity emitted by the PSP depends on the partial pressure of oxygen and directly relates to the pressure of the surrounding gas containing oxygen. Several authors such as

Han et al. [1], Zhang and Jaiswal [35], and Zhang and Fox [36] have discussed the methodology of PSP. Once the PSP is spayed onto the test surface, a 520 nm band pass filter is used to excite the active molecules in the PSP and return a signal in the yellow wavelength. A 610 nm band pass filter and CCD (Charge-Coupled Device) camera are used to record the emitted light. For film effectiveness, PSP uses a mass concentration principle. Using air (79% nitrogen) as the mainstream gas and nitrogen as the coolant, the film effectiveness can be expressed in terms of oxygen concentrations that are measured by the PSP light intensity, as seen in Equation 9.

$$\eta = \frac{C_{\infty} - C_{mix}}{C_{\infty}} \tag{9}$$

Here C_{∞} is the oxygen concentration of the mainstream (near 21%) and C_{mix} is the oxygen concentration of the mainstream-coolant mixture (between 0 and 21 %). As a result, the film effectiveness will be between 0% far downstream of the coolant injection and 100% inside the hole. The mass fraction of the tracer gas in the mixture near the test surface is related to the adiabatic wall temperature for the analogous heat transfer situation.

The test setup consists of the CCD camera with a filter, a strobe light with a filter, and the test surface. A transparent window is located over the test surface, and the CCD camera is mounted above the window. The strobe light is positioned so that maximum excitation of the PSP occurs. The camera records the emitted intensity of the PSP as gray-scale images, which are saved as TIFF files. Using a data reduction program, the intensity image files and calibration data are used to calculate the surface pressure of the test surface. Four images are needed to calculate the film effectiveness: a dark image (no light, no air), a reference image (light on, no air), an air injection image (light on, air on, coolant is air), and a nitrogen injection image (light on, air on, coolant is nitrogen). The air injection image contains information of surface static pressure only, while the

nitrogen injection image contains both the surface static pressure and the oxygen concentration information. Using the ratio of these four images, the oxygen concentration on the test surface downstream of the injection can be separated from the pressure distribution to get the film effectiveness.

Thermocouples

The film effectiveness can also be found by using thermocouples to determine the local wall temperature of the test surface. Thermocouples are embedded flush with the test surface, and a thin foil is placed over the thermocouples to produce a smooth, continuous surface. The effectiveness measurements are made with the mainstream at ambient temperature, the coolant air heated, and the test surface unheated. Because the test surface is unheated and well insulated, it is assumed to be adiabatic. Therefore the local wall temperature at steady state conditions measured by the thermocouples is now the adiabatic wall temperature, T_{aw}. Since the test surface is adiabatic, there is no heat transfer at the surface. As a result, the local film temperature, T_f, is equal to the corresponding adiabatic wall temperature, T_{aw}. Now Equation 2 can be used to calculate the film cooling effectiveness.

$$\eta = \frac{T_{aw} - T_m}{T_c - T_m} \tag{2}$$

This method of calculating the film effectiveness has been used by several researches such as Ou et al. [25] and Mehendale and Han [37].

Infrared Thermography

Infrared thermography (IR) is used to provide full-surface temperature maps for both high and low temperatures. To obtain the effectiveness data, the test surface must be of

low thermal conductivity to reduce any conduction losses. The emissivity of the surface must also be known in order for the IR camera to read the correct temperatures. Once the IR camera has been calibrated with thermocouples, it can provide a two dimensional temperature distribution of the test surface. The measured surface temperatures are assumed to be adiabatic wall temperatures due to the low conduction losses. Then T_f in Equation 1 is replaced by T_{aw}, or the adiabatic wall temperature, as in Equation 2.

$$\eta = \frac{T_{aw} - T_m}{T_c - T_m} \tag{2}$$

This measurement technique has been used by Dittmar et al. [14], Saumweber et al. [17], and Gritsch et al. [32].

INSTRUMENTATION

A low speed suction type wind tunnel with a maximum velocity of 34 m/s is used for this study. Detailed information on the wind tunnel can be found in Young et al. [38]. The 4:1 contraction ratio of the nozzle produces uniform flow at the entrance of the test section. The wind tunnel has an inlet cross-section of 60.96 cm x 30.48 cm. A 5 μm cotton filter and packed plastic straw flow straightener box are installed in front of the nozzle inlet. The test channel cross section is 30.48 cm x 15.24 cm. The wind tunnel operates in the suction mode with a 5.6 kW axial blower. A central air-conditioning system maintained mainstream temperature at 28°C. A turbulence grid is set upstream of the test surface which creates a turbulence intensity of 6 percent. It is composed of a square mesh of aluminum tubes—thirteen tubes in the vertical direction and seven tubes in the horizontal direction. The tube diameters are each 0.635 cm. Figure 3 shows a 3-D model of the wind tunnel.

The coolant air, supplied from a compressor or nitrogen tank depending on the measurement technique, passes through a flow control valve and orifice flow meter. The coolant then passes through a 5 kW pipe heater and bypass valve before it enters the air plenum, which is directly underneath the film cooling plate.

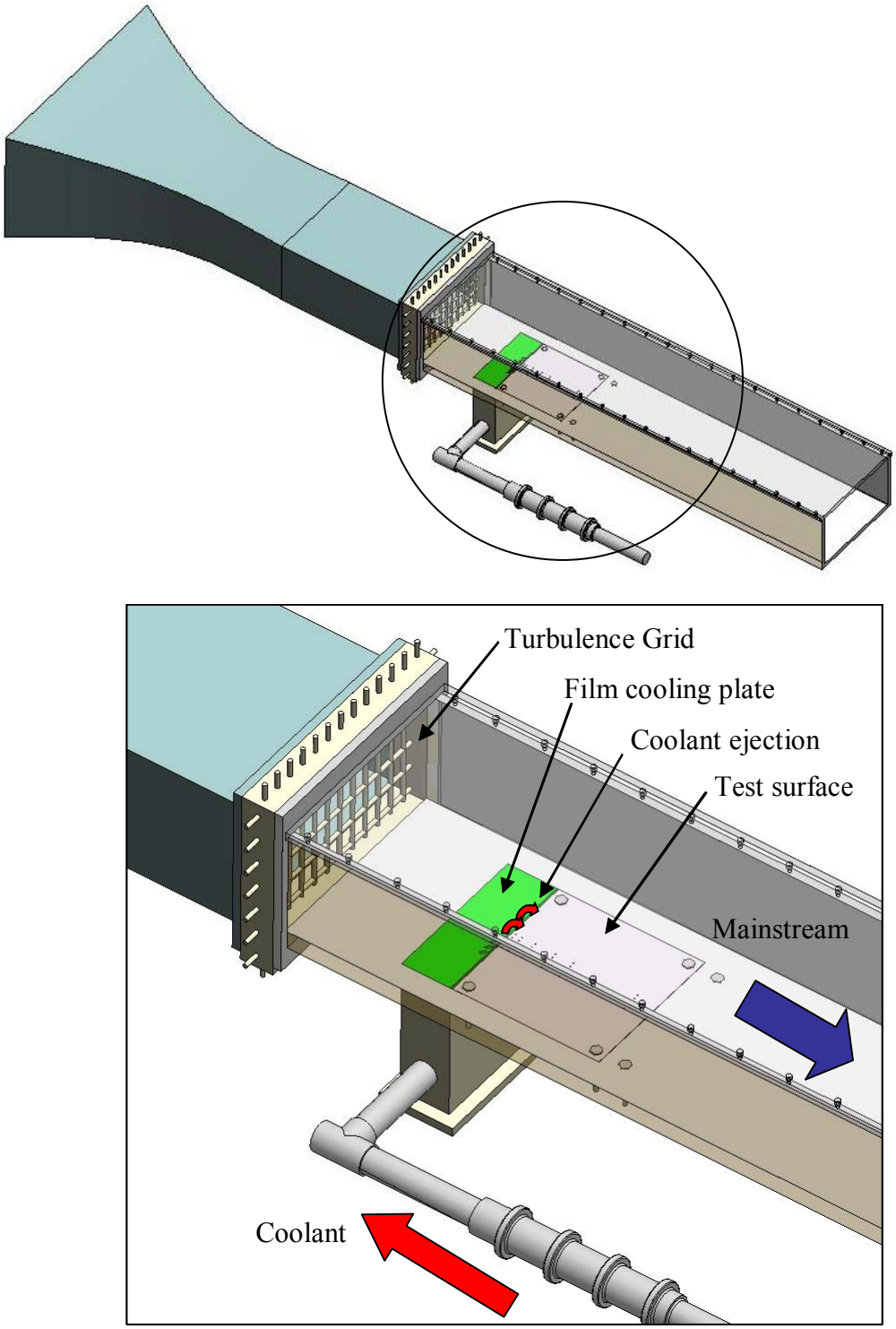

Figure 3. 3-D model of wind tunnel

For all measurement techniques, a T-type thermocouple is used to measure the inlet mainstream temperature. For the coolant temperature, two T-type thermocouples are attached on the bottom of the film cooling plate — one at the each entrance of the two outside holes. The thermocouple readings are measured by a Fluke 2285B Data Logger. Figure 4 shows a detail view of the experimental setup for the liquid crystal and PSP technique.

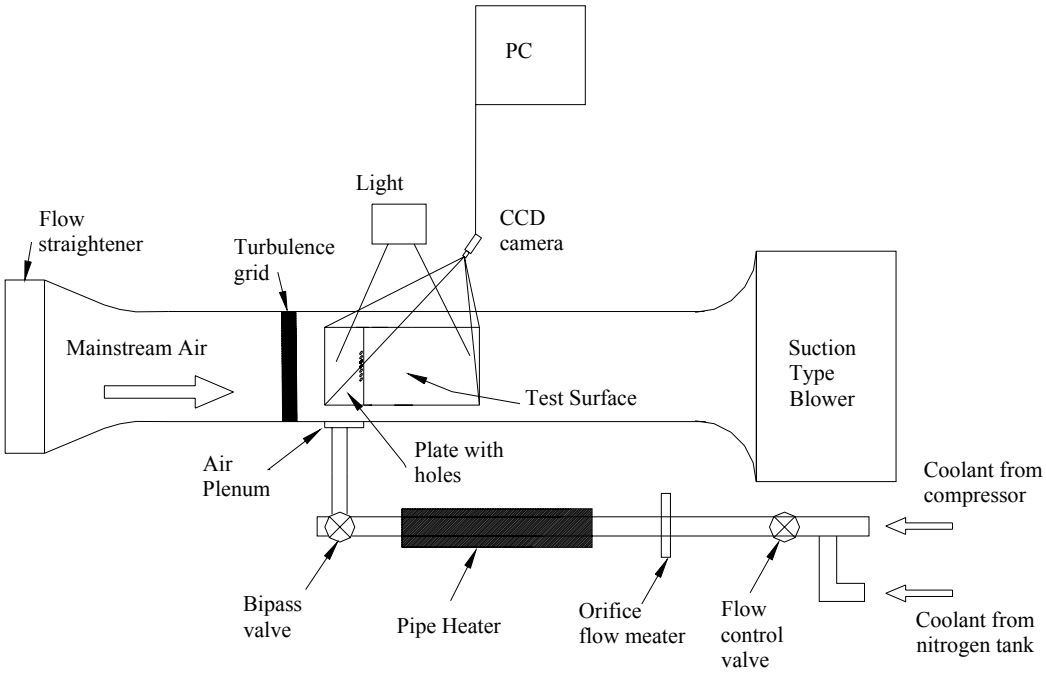

Figure 4. Experimental setup for steady-state liquid crystal, transient liquid crystal, and PSP measurement techniques

Figure 5 shows a detailed view of the setup for the thermocouple and IR technique.

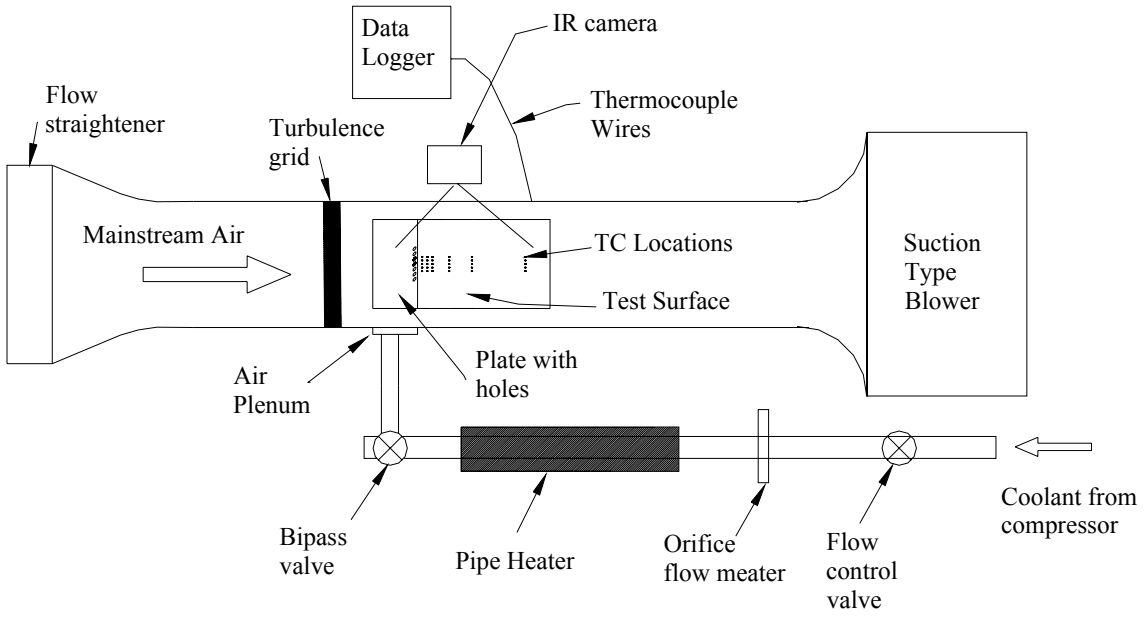

Figure 5. Experimental setup for thermocouple and IR measurement techniques

Five hole geometries are considered for this study:

- Plate 1 – compound angle cylindrical holes
- Plate 2 – axial angle laid-back fan-shaped holes
- Plate 3 – compound angle laid-back fan-shaped holes
- Plate 4 – axial angle conical holes
- Plate 5 – compound angle conical holes

The film cooling plates are 9.0 in x 3.0 in x 0.6 in. Each plate consists of a single row of seven holes, and the downstream edge of the holes is 1.6 mm from the downstream edge of the plate. Plates 1 and 2 were made by the electrical discharge machining (EDM) process and are made out of stainless steel. Plate 1 consists of cylindrical holes with a

diameter of 4 mm. The spanwise spacing of the holes are 12 mm (3D). They have a 30º streamwise angle (θ) and a 45º spanwise angle (β). Plate 2 consists of laid-back fan-shaped holes that expand 10º in the spanwise directions and 10º in the streamwise direction. These holes have a 30º streamwise angle and a lateral spacing of 15 mm (3.75D).

Plates 3 – 5 were made by the stereo lithography (SLA) process and are made of Somos® 9120 epoxy photopolymer. Plate 3 consists of holes identical to Plate 2, except that they have a 45º spanwise angle. Plate 4 consists of conical expanded holes. These holes expand 4º in all directions (360º of the hole). They have a 30º streamwise angle and a spanwise spacing of 15mm (3.75D). Plate 5 has holes identical to Plate 4, but they also have a 45º spanwise angle. Table 2 summarizes the hole geometries of each plate.

Table 2. Summary of shaped hole geometries.

Plate	hole type	injection angle type	compound angle	axial angle	D [mm]	total L/D	cylindrical L/D	breakout L/D
1	cylindrical	compound angle	45º	30º	4	9.92	9.92	N/A
2	fan-shaped	axial angle	0º	30º	4	7.5	4.3	3.2
3		compound angle	45º	30º to compound plane	4	7.5	5	2.5
4	conical	axial angle	0º	30º	4	7.5	5.375	2.125
5		compound angle	45º	30º to compound plane	4	7.5	5.375	2.125

Figure 6 shows a detailed view of each hole geometry. The film cooling plate is screwed onto the air plenum so that the top surface of the plate rests flush with the bottom surface of the wind tunnel. The film cooling holes are located 21.75 cm (x/D = 54.4) from the turbulence grid. A 9.0 in x 9.0 in x 0.5 in Plexiglas piece is attached directly downstream of the film cooling plate and is also flush with the bottom surface of the wind tunnel.

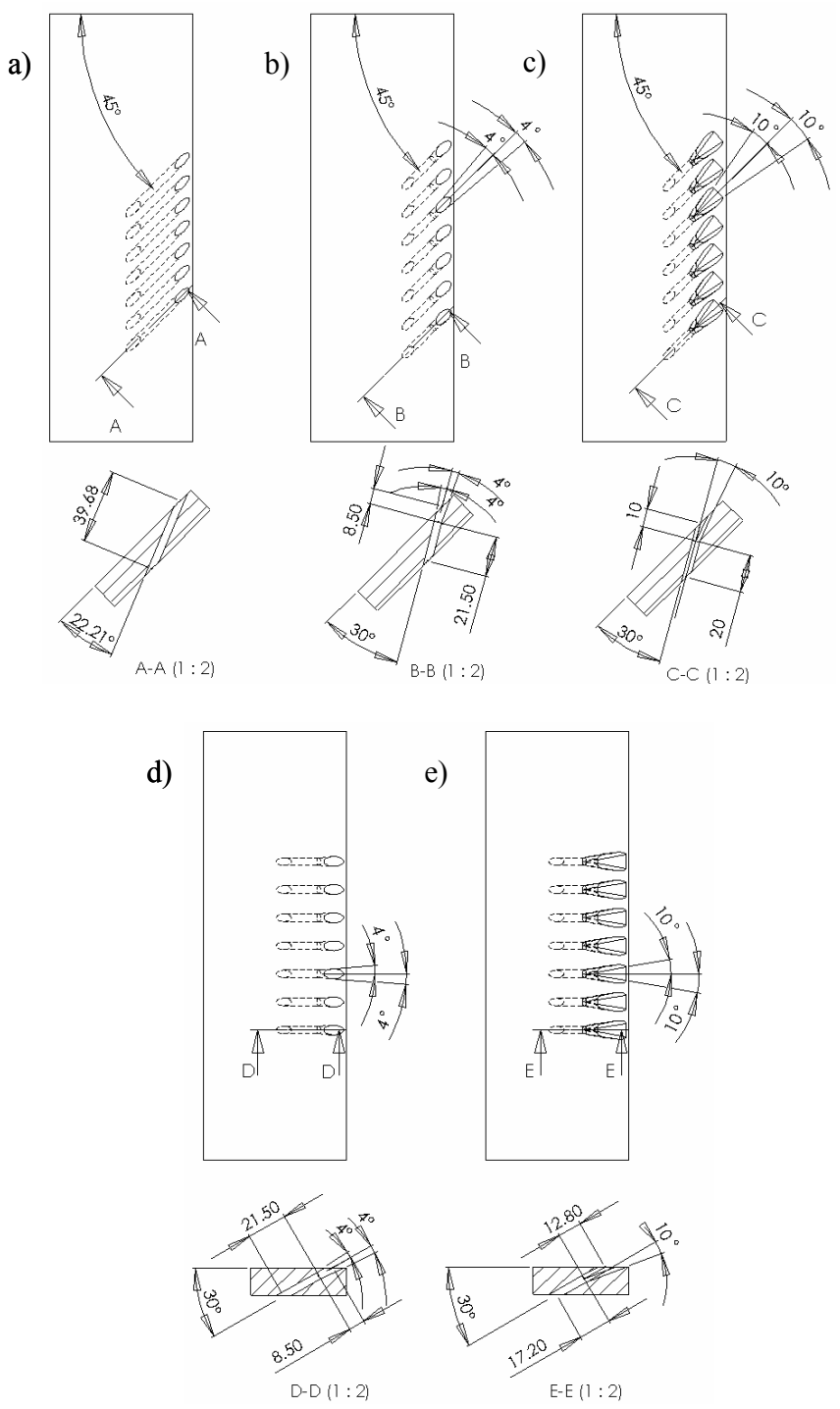

Figure 6. Overview of film cooling hole geometries: a) cylindrical with compound angle, b) conical with compound angle, c) laid-back fan-shaped with compound angle, d) conical with axial angle, and e) laid-back fan-shaped with axial angle

In Part 1 of this study, two interchangeable Plexiglas pieces are used as the downstream test surface depending on the measurement technique. The first piece, as seen in Figure 7, is a smooth surface and is used for the liquid crystal and PSP measurement techniques.

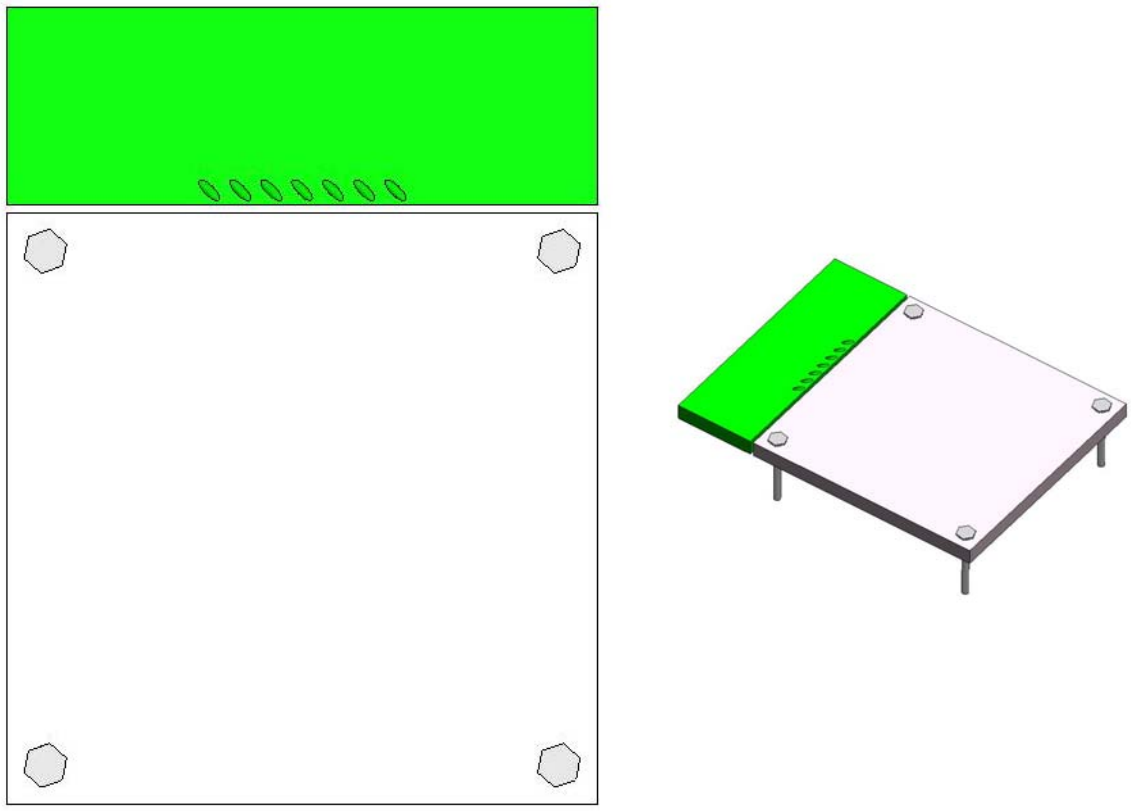

Figure 7. Smooth test surface piece used for the liquid crystal and PSP techniques

The second piece, as seen in Figure 8, is used for the thermocouple and IR measurement techniques. It has five rows of six holes drilled for the 30 thermocouples. The hole diameters are all 1/16 in. The 30 gauge T-type thermocouples are inserted from the bottom of the Plexiglas so that the welded bead of the thermocouple is flush with the top surface. The thermocouples are glued into place with a two part Epoxy adhesive. The test surface and thermocouple beads are then covered with a thin foil to ensure a smooth

continuous test surface. All thermocouples are in contact with the thin foil. The X/D spacing of the thermocouple rows is 2, 4.5, 10, 18, 25, and 50.

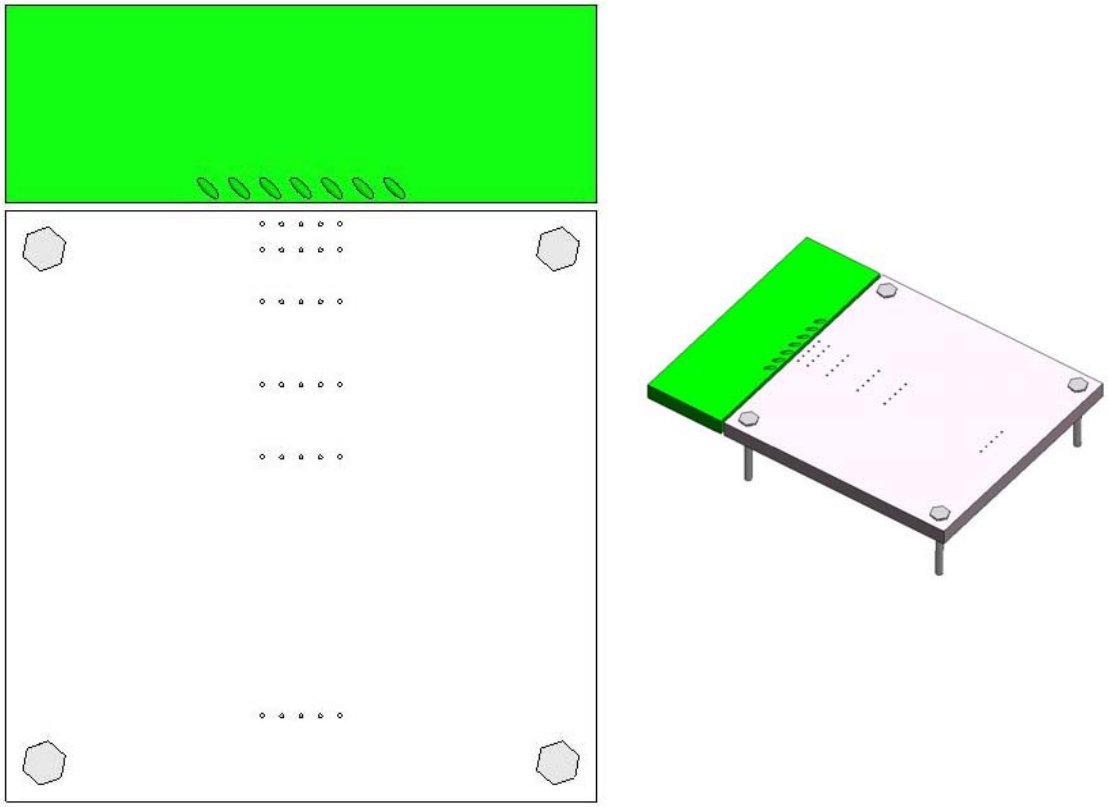

Figure 8. Test surface piece used for the thermocouple and IR techniques

Part 2 of this study uses only the PSP measurement technique. Therefore, only the smooth Plexiglas test surface is needed for these experiments.

RESULTS AND DISCUSSION

Part 1: Comparison of Effectiveness Measurement Techniques

For Part 1, the effectiveness results for each measurement technique are first presented. The overall comparison between the measurement methods is then discussed at the end of this section.

Steady State Liquid Crystal Thermography

For the steady state method, the 20ºC bandwidth liquid crystals (R34C20W, Hallcrest) were used to measure the adiabatic wall temperature of the test surface. A calibration was obtained to find the relationship of the temperature versus the hue, or color of the liquid crystals. A foil heater was placed under a 0.635 cm copper plate. Because the color display of the liquid crystals is dependent upon the background color, the copper plate was first sprayed with a black paint (BBG1, Hallcrest) that was also used as the background color of the test surface. After the black paint was dry, the 20ºC bandwidth liquid crystal was uniformly sprayed onto the copper plate. An input voltage was applied to the foil heater so that the surface temperature measurements of the copper plate were taken at increments of 0.6ºC. Enough time was allowed between each increment so that the temperature was steady state at each temperature step. A thermocouple was used to measure the surface temperature, and the corresponding color of the liquid crystals was recorded to a computer. For each temperature step, the hue was calculated from the stored image, and the hue versus temperature relationship was obtained. Figure 9 shows the results of the calibration.

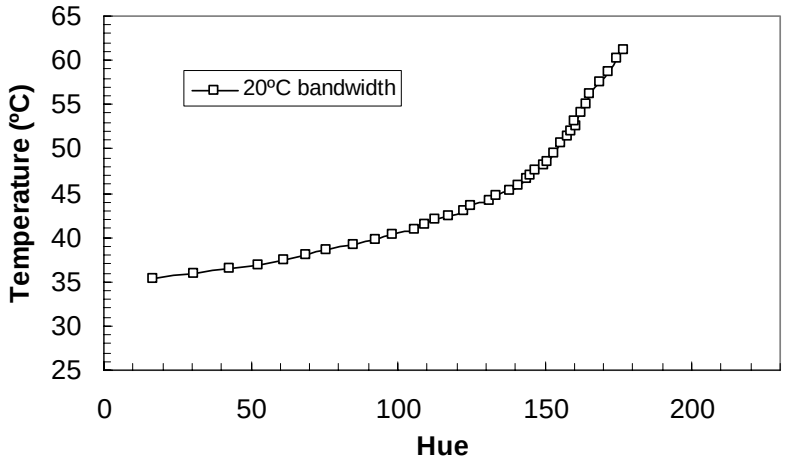

Figure 9. Calibration curve for the 20ºC bandwidth liquid crystal

For the steady state test, the coolant air at the inlet of the film cooling holes was heated to about 40ºC, and the mainstream air was at room temperature (22.2ºC). After an hour, when steady state conditions were reached, the color of the liquid crystals on the test surface was recorded by a RGB color charge-coupled device (CCD) camera with 16-bit color frame grabber board. The hue was calculated for every pixel of the stored image. Using the calibration curve, the local steady-state adiabatic wall temperature was determined.

Figure 10(a-d) shows the local effectiveness results for the cylindrical holes with a compound angle (Plate 1) for M 0.3, 0.6, 1.2, and 1.8, respectively. The blowing ratio was based upon the inlet hole area for all cases.

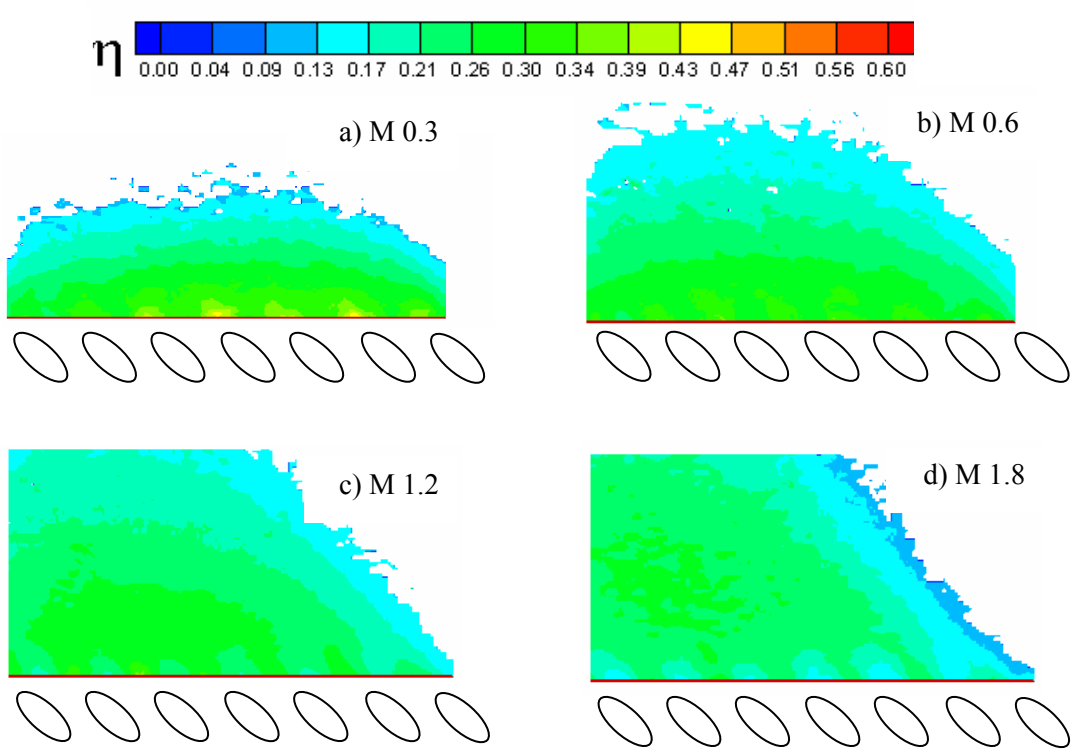

Figure 10. Local effectiveness plots of Plate 1 using the steady state liquid crystal method for blowing ratios of (a) 0.3, (b) 0.6, (c) 1.2, and (d) 1.8

The red line represents the end of the metal plate with the film cooling holes and the start of the Plexiglas test plate. No data could be obtained near the holes because of the high conductivity of the metal plate. The gap from the downstream edge of the film cooling holes the upstream edge of the test plate is 1/16 in.

Seen from Figure 10, as the blowing ratio increases, the effectiveness of the film coolant tends to cover more area downstream of the holes. The higher blowing ratios cover more distance in the downstream direction than the lower blowing ratios. For the lower blowing ratios, the mainstream pushes the coolant towards the downstream direction, which creates more uniform coverage in the lateral direction. However, the higher blowing ratios increase the coolant momentum, so the coolant flow is not so easily deflected by the mainstream. As a result, the lateral coverage of the coolant is not as

uniform. Therefore, optimizing the blowing ratio involves finding a balance between uniform lateral coverage and the distance covered downstream of the holes.
The high momentum of the coolant can also cause a separation from the surface, as seen in Figure 10(d). The highest effectiveness is not immediately downstream of the holes. The coolant penetrates into the mainstream and then is pushed back towards the surface. This location of reattachment shows the highest effectiveness. The separation can be easily seen when the effectiveness is laterally averaged.

Figure 11(a) shows the averaged effectiveness for the four blowing ratios. The data is averaged for the three middle holes, as seen in Figure 11(b). The effectiveness data is plotted for two different non-dimensional distances. The first non-dimensional distance is x/MS – the downstream distance (x) divided by the blowing ratio (M) and equivalent slot width (S). This parameter is used to try to correlate the data for all blowing ratios onto one curve. The second non-dimensional distance is x/D – the downstream distance divided by the inlet hole diameter. The downstream edge of the holes is where x = 0. Because no data is available near the holes for the steady state method, the plots do not begin at zero.

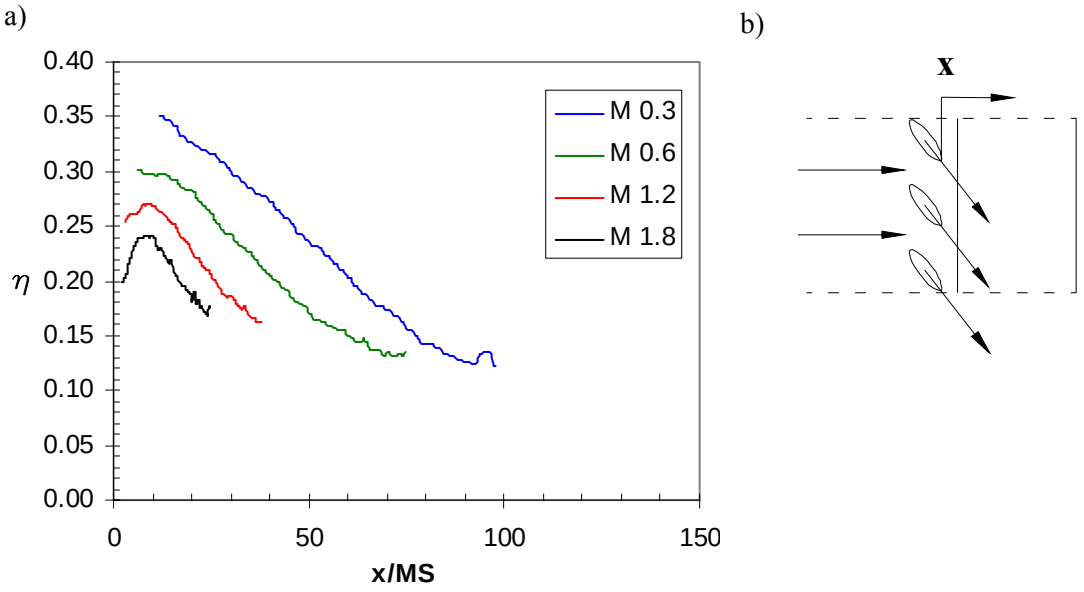

Figure 11. (a) Laterally averaged effectiveness of Plate 1 using the steady state liquid crystal method, (b) area of the 3 middle holes of Plate 1 used to average the effectiveness

Separation is noted for M = 1.8 and 1.2. As the coolant exits the holes, the effectiveness is low. It increases to a maximum, which is where the coolant reattaches to the surface. Then as the coolant travels even further downstream, it gradually looses its effectiveness as it mixes with the mainstream. As seen from the figure, the curves for each blowing ratio do not correlate well with each other.

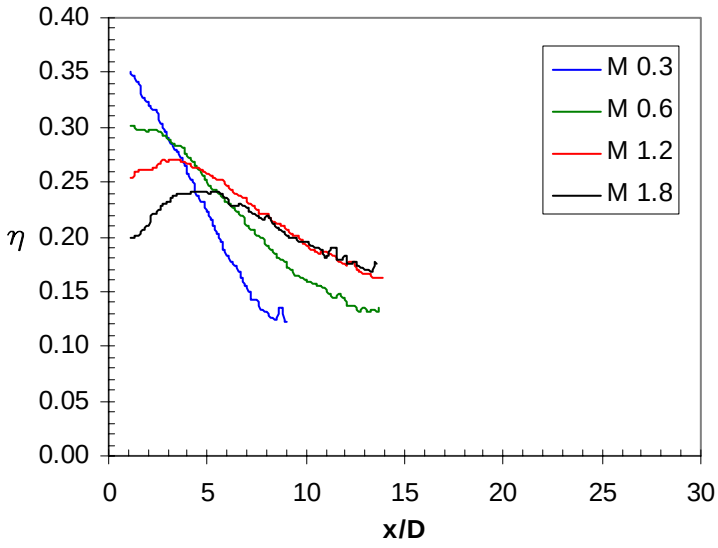

Figure 12. Laterally averaged effectiveness of Plate 1 using the steady state liquid crystal method plotted versus x/D

Figure 12 plots the laterally averaged effectiveness versus the x/D parameter. From open literature, the optimum blowing ratio for cylindrical holes with compound angles is around M = 0.5. However, for this test, there were some conduction effects for the lower blowing ratios of M = 0.3 and 0.6. The hot coolant air at steady state conditions heated up the metal film cooling plate. Some of this heat was transferred at the interface between the film cooling plate and the Plexiglas test plate. As a result, the surface temperature immediately downstream of the holes was higher due to the conduction effect, which also increased the effectiveness values.

This conduction effect can be seen in both steady state methods that involve heating: the steady state liquid crystal, the thermocouples, and the IR method. For example, the case of M 0.3 has lower effectiveness than that of M 1.8, as shown by the PSP, which means the wall temperature is also lower for M 0.3. However, all blowing ratio cases are run with the same coolant and mainstream temperatures. Therefore the temperature difference between the film cooling plate and the test plate is higher for M 0.3, and an increased temperature difference means an increased heat loss. A diagram is shown in Figure 13. With more heat conducted into the test plate, the wall temperature will

increase making the effectiveness greater than the true value. In other words, the effectiveness values for the low blowing ratio cases have a greater percent error than the high blowing ratio cases.

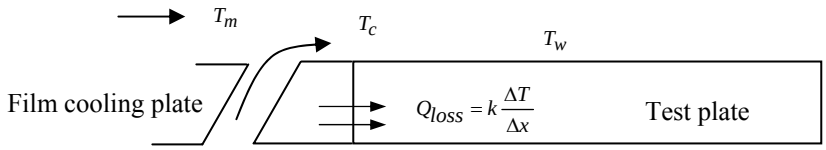

Figure 13. Temperature model of test section showing the conduction effect on effectiveness measurements

An uncertainty analysis like that described in Kline and McClintock [39] was performed on the steady state liquid crystal method. The individual uncertainties in the mainstream temperature (T_m) was ± 0.2ºC; the coolant temperature (T_c) was ± 0.2ºC, and the color change temperature of the liquid crystal (T_w) was ± 0.2ºC. The results showed the effectiveness values to an averaged uncertainty of ± 10%. The uncertainty value was larger for low effectiveness levels, though. For example, the uncertainty value was ± 0.014 for $\eta = 0.2$ but ± 0.015 for $\eta = 0.05$.

Transient Liquid Crystal Thermography

For the transient method, the 20ºC bandwidth liquid crystal (R34C20W, Hallcrest) was used to measure the initial temperature of the test surface. The 5ºC bandwidth liquid crystal (R29C5W, Hallcrest) was used to measure the color changing time. A calibration like the one used for the steady state method was performed to find the relationship of the temperature versus the hue for each bandwidth of liquid crystal. A foil heater was placed under a 0.635 cm copper plate that was first sprayed with a black paint (BBG1, Hallcrest). After the black paint was dry, the 20ºC band width liquid crystal was

uniformly sprayed onto the copper plate. An input voltage was applied to the foil heater so that the surface temperature measurements of the copper plate were taken at increments of 0.6ºC. Enough time was allowed between each increment so that the temperature was steady state at each temperature step. A thermocouple was used to measure the surface temperature, and the corresponding color of the liquid crystals was recorded to a computer. For each temperature step, the hue was calculated from the stored image, and the hue versus temperature relationship was obtained. This method was repeated for the 5ºC bandwidth liquid crystal. Figure 14 shows the results of the calibration for both the 20ºC and 5ºC bandwidths.

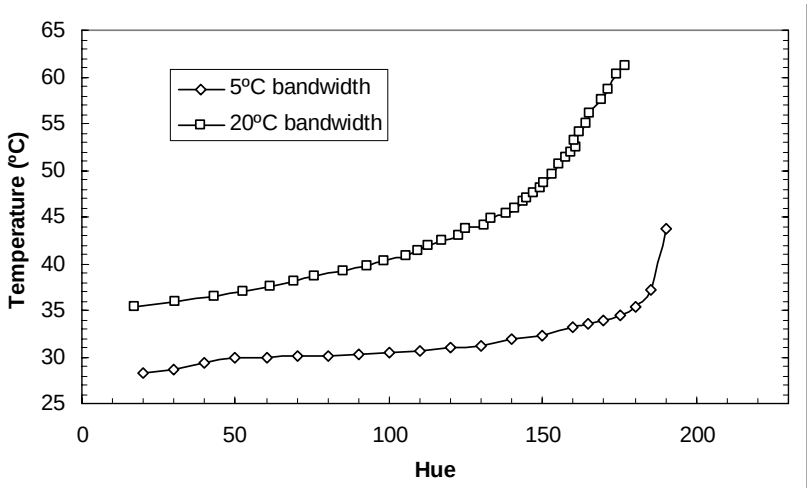

Figure 14. Calibration curve of the two bandwidths used for the transient liquid crystal method

For the transient test, the test surface, sprayed with the 20ºC bandwidth, was heated for an hour to a desired initial temperature (40.5ºC). The CCD camera then recorded the color of the test surface, and the hue was calculated for every pixel of the stored image. Using the calibration curve, the initial surface temperature was determined.

Once the initial temperature measurement was made, the 20ºC bandwidth liquid crystals were removed from test surface, and the 5ºC bandwidth was applied. The test surface was then heated for about an hour so that the reference temperature matched that of the

initial temperature measurement. This reference temperature was measured by a thermocouple located about five hole diameters downstream and about four hole diameters to the outside of the first hole. When the reference temperature reached the desired value, the CCD camera, wind tunnel, and coolant were simultaneously switched on. The color change of the liquid crystal was recorded at the speed of 2 frames per second. The run time of the test was short enough (less than 3 minutes) to make a semi-infinite solid assumption. For every pixel at each image, the hue was evaluated and used to calculate the time change from the initial condition to a desired hue value of 115, which corresponded to a temperature of 30.2ºC. This hue value of 115 was selected because it corresponded to the green color, which has the brightest intensity and is best detected by the CCD camera. Two similar tests were run with different coolant temperatures. The first test had the coolant and mainstream at room temperature, while the second test had the mainstream at room temperature and the coolant heated to 35ºC. Then, using Equations 7 and 8, the local heat transfer coefficient and film cooling effectiveness were calculated.

Figures 15(a-d) show the transient liquid crystal local effectiveness results for the cylindrical holes with a compound angle (Plate 1) for M 0.3, 0.6, 1.2, and 1.8, respectively.

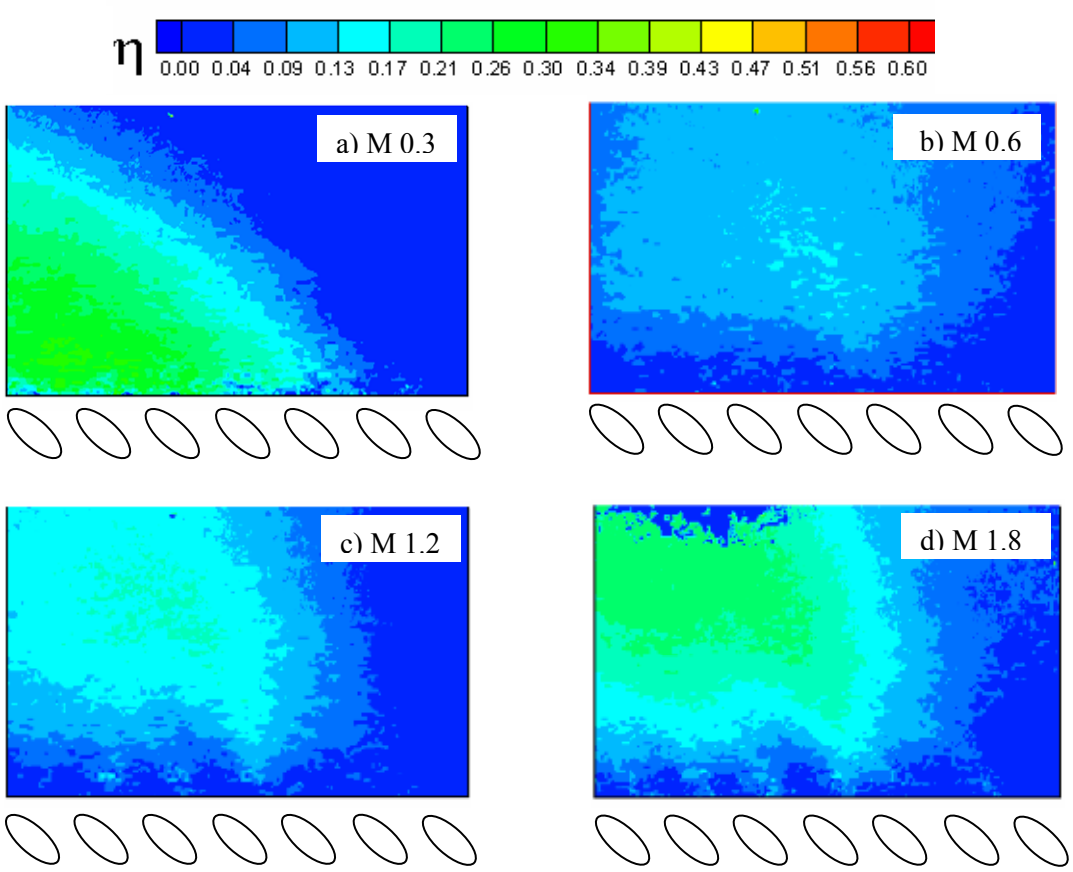

Figure 15. Local effectiveness plots of Plate 1 using the transient liquid crystal method for blowing ratios of (a) 0.3, (b) 0.6, (c) 1.2, and (d) 1.8

Just like the steady state method, the transient method was not able to obtain data in the near hole region due to the high conductivity of the metal plate. As seen from Figure 15, the higher blowing ratios have a higher effectiveness further downstream than the lower blowing ratios. The exception is the lowest blowing rate of M 0.3. Coolant separation can be seen for blowing ratios of M = 0.6, 1.2, and 1.8. The effectiveness is low immediately downstream of the holes, and then it increases as the coolant reattaches to the surface. Separation occurs when the coolant has too much momentum as it exits the holes. The lowest blowing rate of M = 0.3 seems unusually high. The test was repeated several times, but it resulted in the same effectiveness levels.

Figures 16 and 17 plot the averaged effectiveness values of the transient liquid crystal method versus the x/MS parameter and the x/D parameter, respectively.

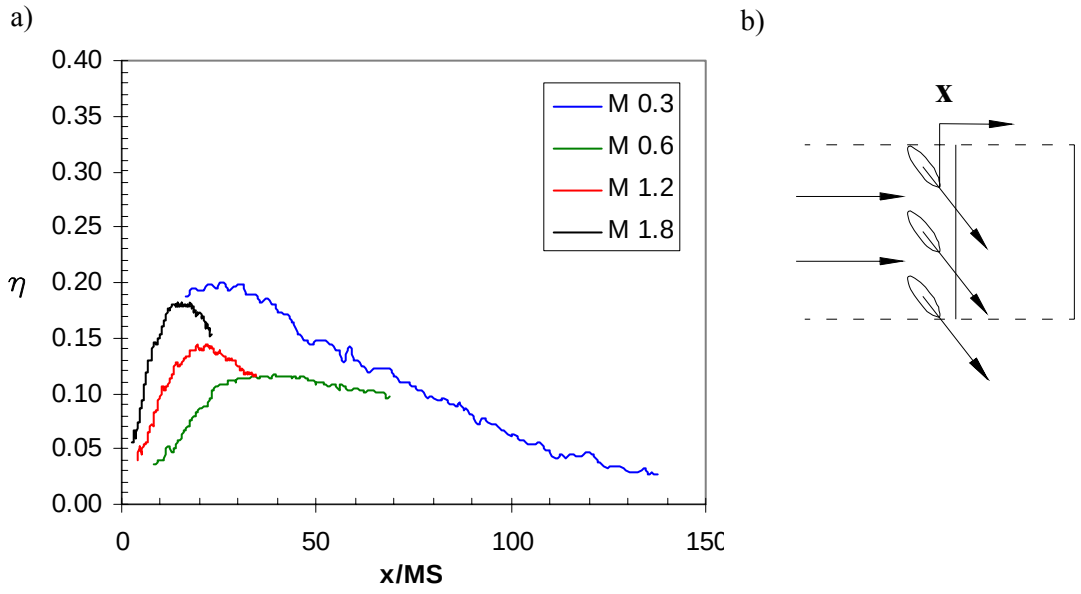

Figure 16. (a) Laterally averaged effectiveness of Plate 1 using the transient liquid crystal method, (b) area of the 3 middle holes of Plate 1 used to average the effectiveness

Like the steady state liquid crystal method, the laterally average effectiveness was averaged over an area that spanned the three middle holes of the film cooling plate, seen in Figure 16(b). The transient liquid crystal results are somewhat different that the steady state liquid crystal. For example, the blowing ratio of M = 0.6 shows the lowest effectiveness of all four blowing ratios, which does not agree with open literature. Figure 16 tries to correlate the effectiveness data for all blowing ratios of Plate 1 with the x/MS parameter, but there is a large variation between the data sets.

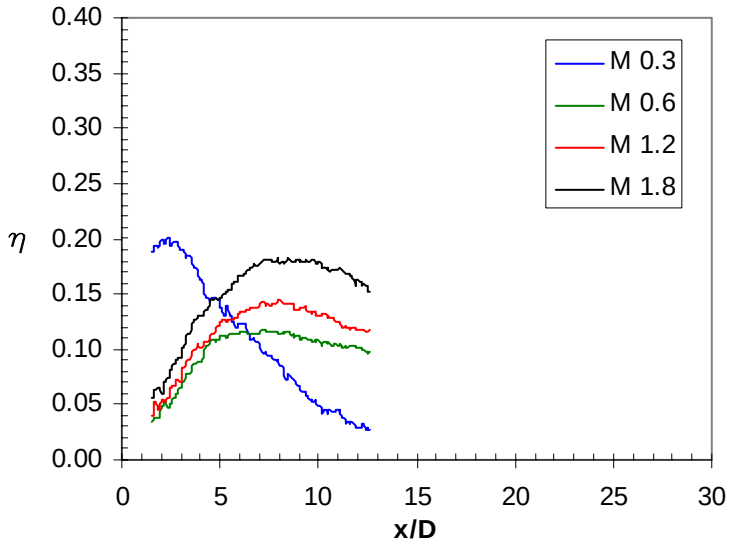

Figure 17. Laterally averaged effectiveness of Plate 1 using the transient liquid crystal method versus the x/D parameter

Looking at Figure 17, the transient liquid crystal method showed the lowest blowing ratio to have the highest effectiveness for the near hole region. The peak effectiveness for M = 0.3 was 0.2, which occurred at x/D = 2.5. However, the effectiveness quickly dropped to 0.05 at x/D = 10. The other three blowing ratios showed the separation and reattachment of the coolant. The case for M = 1.8 had a peak effectiveness of 0.18 located at x/D = 7. The case for M = 0.6, though, only had a peak effectiveness of 0.12, which does not correspond to the data of the steady state liquid crystal or to any data in open literature.

The uncertainty analysis described by Kline and McClintock [39] was performed on the transient liquid crystal method. Individual uncertainties used in the calculation of the heat transfer coefficient included the time of the color change (t = ± 0.2 sec), the mainstream temperature (T_m = ± 0.2ºC), the initial temperature (T_i = ± 0.2ºC), the color change temperature (T_w = ± 0.2ºC), and the wall material properties (α/k^2 = ± 3%). The average uncertainty of the heat transfer coefficient was estimated to be ± 8%. The uncertainty of the film cooling effectiveness, which included the uncertainties of the heat

transfer coefficient, was ± 11%. Radiation losses are assumed to be minimal because the entire walls of the test duct are heated by the mainstream at fairly uniform temperatures. Conduction losses are small because the transient test time is short and the test surface material is made of material with low thermal conductivity. However, the uncertainty near the upstream edge of the Plexiglas test surface could be much higher than 11% due to the assumption of one-dimensional conduction over the entire test surface.

PSP

The PSP test setup included a CCD camera, a light source, the test surface, and the film cooling plate. The camera was mounted directly overhead of the test surface, which could be viewed through a transparent window. The air and the nitrogen were delivered to the air plenum through a series of regulator valves, pipes, and a flow meter. Operating conditions of the suction type wind tunnel fall below atmospheric pressure at room temperature. As a result, the PSP was calibration at room temperature for pressures between vacuum and 101.3 kPa. Atmospheric pressure was used as a reference pressure for the calibration curve, which is plotted as the reverse intensity ratio versus the pressure ratio. To perform the calibration, a sealed chamber with a window was placed in the same location of the test surface so that the distance and angle from the CCD camera and light source was identical to that of the test surface. A vacuum pump and valve were used to regulate the pressure inside the chamber. A small plate (2 in x 2 in) made of the same material as the test surface was painted with PSP and placed in the calibration chamber. Once the chamber was sealed and checked for any leaks, 200 images were taken for each pressure level. A computer program then averaged the intensities of each set of the images to determine the intensity ratio and pressure ratio relationship. Figure 18 shows the results of the calibration curve.

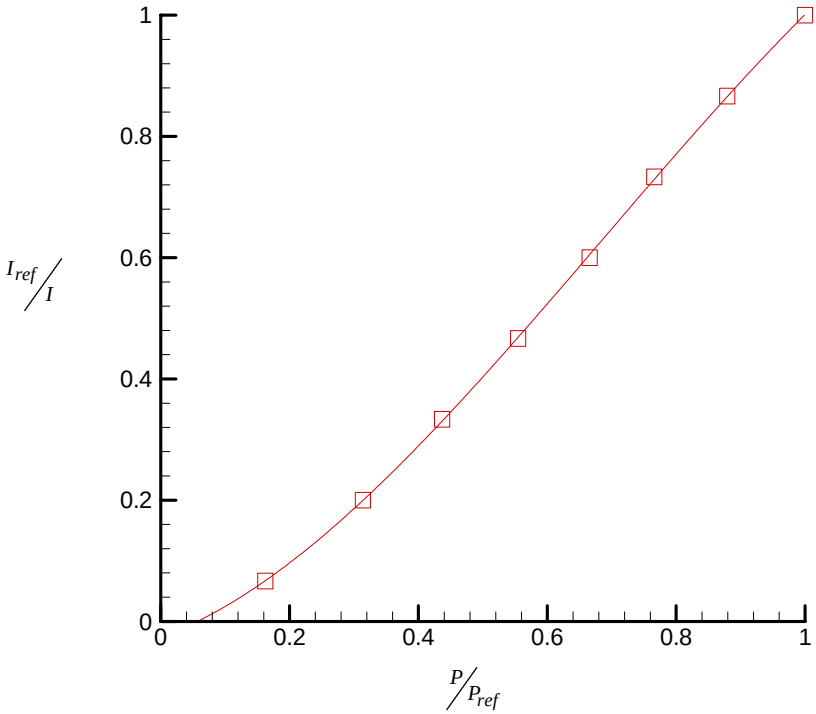

Figure 18. Calibration curve used for the PSP method

The pressure sensitive paint was then uniformly sprayed onto the test surface and the film cooling plate. With the calibration curve, the measured intensities are converted to the partial oxygen concentrations on the test surface. Equation 9 was then used to calculate the film cooling effectiveness.

Figure 19(a-d) shows the contour plots of the effectiveness for cylindrical compound holes (Plate 1) at the blowing ratios of M 0.3, 0.6, 1.2, 1.8.

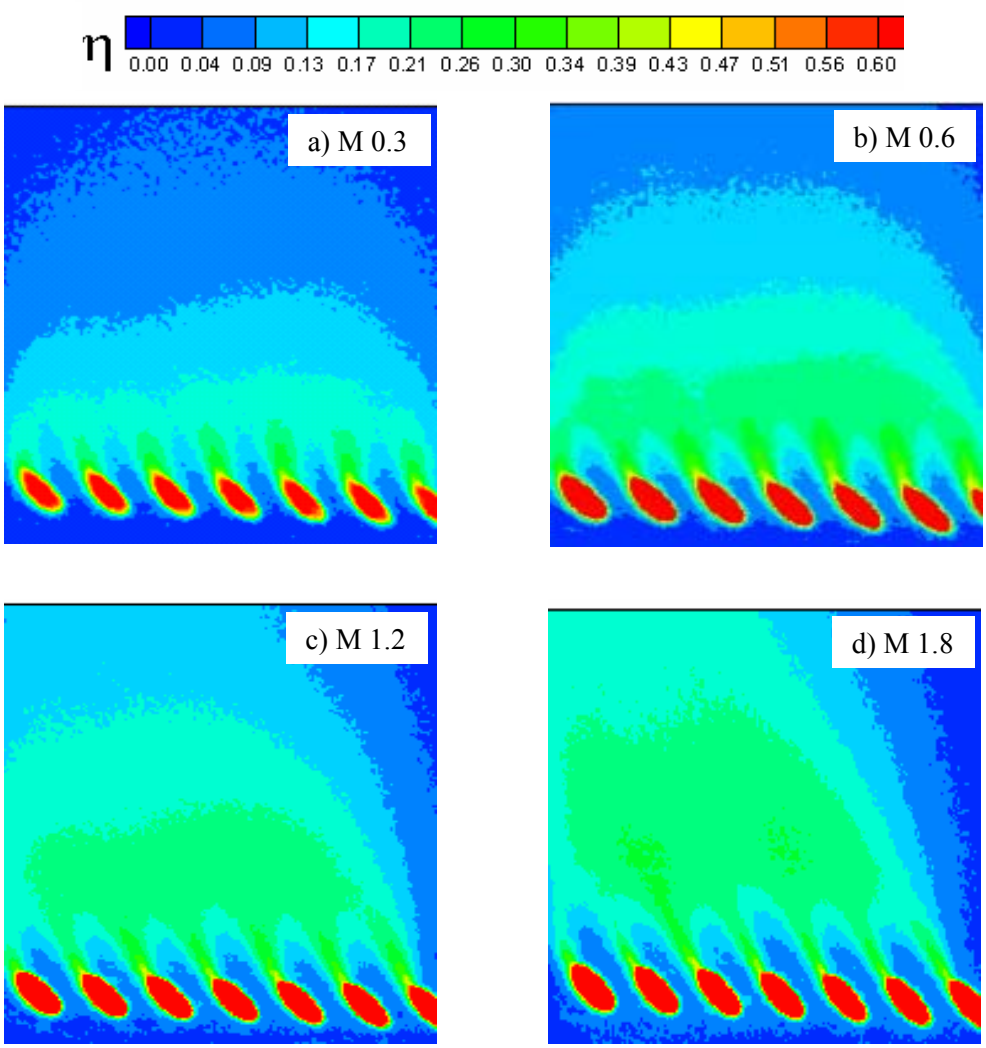

Figure 19. Local effectiveness plots of Plate 1 using the PSP method for blowing ratios of (a) 0.3, (b) 0.6, (c) 1.2, and (d) 1.8

As seen in Figure 19(a), the trace of the coolant for M = 0.3 does not extend very far downstream. The coolant jets quickly mix with the mainstream air, and as a result, the effectiveness quickly dissipates. For M = 0.6 (Figure 19(b)), the trace of the jets has the most lateral coverage. For the near hole region, M = 0.6 shows the highest effectiveness.

It is also seen that as the blowing ratio increases (Figures 19(c) and 19(d)), the momentum of the coolant increases. The jets penetrate into the mainstream as they exit the holes, which result in less coverage for the region around the holes. The effectiveness for these blowing ratios is low near the holes and then increase downstream of the holes. This suggests a reattachment of the coolant jets. The case of M = 1.8 shows a strong jet separation and reattachment, but the effectiveness in the far downstream region remains higher than the lower blowing ratio cases.

To see the effects of the blowing ratios more clearly, Figure 20 plots the laterally averaged effectiveness for each case. The effectiveness is averaged for the three middle holes of the plate, as seen in Figure 20(b).

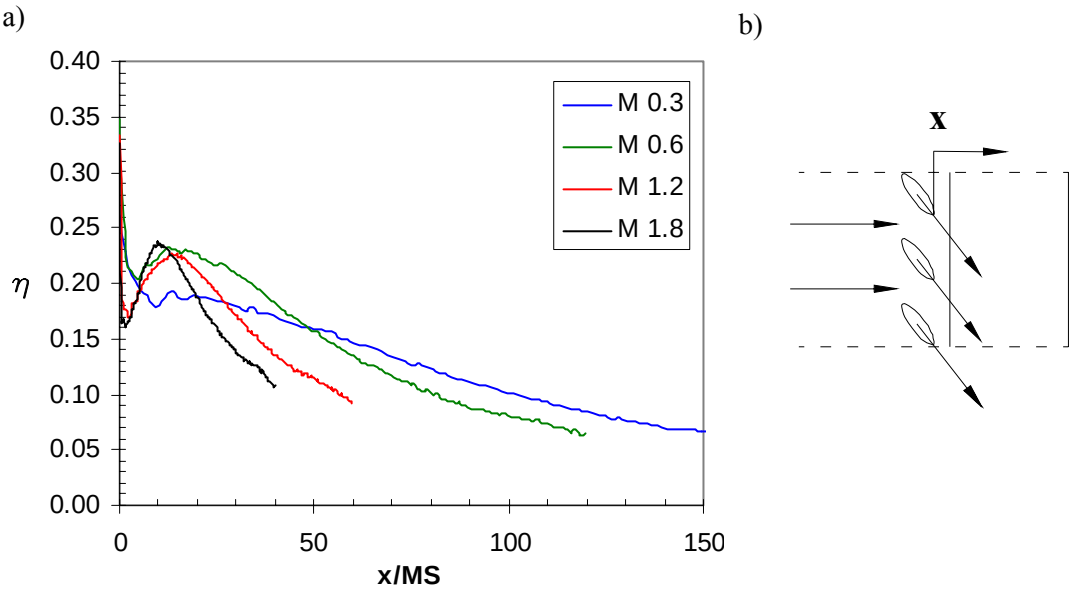

Figure 20. (a) Laterally averaged effectiveness of Plate 1 using the PSP method, (b) area of the 3 middle holes of Plate 1 used to average the effectiveness

Examining the chart shows the lower blowing ratios to have the highest effectiveness at the near hole region. The separation of the coolant for the higher blowing ratios can be seen by the immediate decrease of effectiveness and then quickly increasing as the jets reattach to the surface. The case of M = 0.6 has the same peak effectiveness as the case of M = 1.8, which is suggests that more coolant is not necessarily the optimum choice.

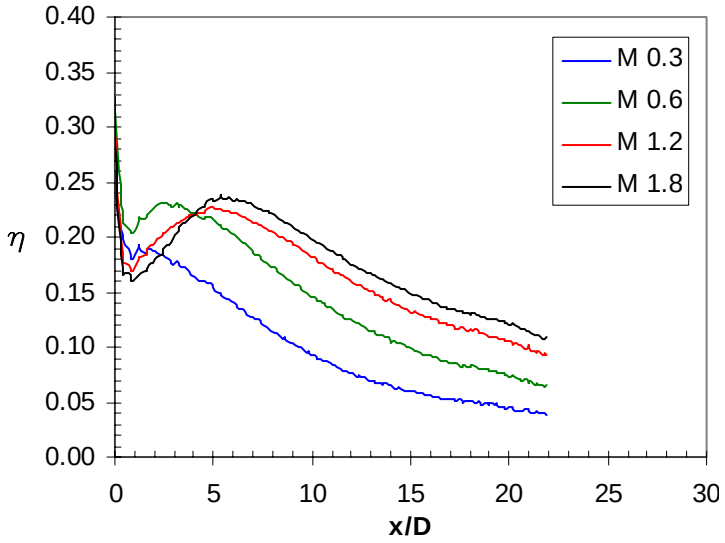

Figure 21. Laterally averaged effectiveness versus the x/D parameter of Plate 1 using the PSP method

Figure 21 shows the averaged effectiveness versus the x/D parameter. From this figure, the peak effectiveness for M = 0.6 occurs at two hole diameters downstream. The higher blowing ratios have a peak effectiveness located five to six diameters downstream. Because the lower blowing ratios generate less momentum as the coolant exits the holes, they show a higher effectiveness than the higher blowing ratios at the near hole regions.

The resolution of the PSP shows good data at the near hole regions. The PSP data is not affected by the edges of the holes or sharp corners (ex. the beginning of the test plate). For effectiveness measurements, this is one strong advantage for PSP. Other methods that involve heating will have more uncertainty around these types of areas because of

conduction effects and the 1-D heat transfer assumption, which is made for the transient liquid crystal measurements.

The uncertainty analysis performed on the film effectiveness measurements of the PSP was based on that described in the Kline and McClintock [39]. The uncertainty of the pressure distribution is estimated to be ± 5.9%, and the film effectiveness was estimated to be ± 9.4%. This yielded a deviation of ± 0.055 effectiveness units for the highest laterally averaged cases.

Thermocouples

For the effectiveness measurement using thermocouples, the test surface was replaced with an identical piece that had 30 thermocouples embedded in the surface, as seen in Figure 8. The layout of the thermocouples consisted of six rows of five thermocouples, which spanned the area of the three middle holes of the film cooling plate. The rows of thermocouples were located at x/D distances of 2, 4.5, 10, 18, 25, and 50. With the mainstream at room temperature and the coolant heated to about 40ºC, tests were run for each blowing ratio. Steady state conditions were reached after 45 minutes to an hour. The temperatures for each point were recorded, and Equation 2 was used to calculate the effectiveness.

Because of the limited number of measurement points, a detailed contour plot of effectiveness is not available, which is a disadvantage for the thermocouple measurement. The results are plotted by averaging the effectiveness of the five points at each row. Figure 22 shows these plots versus the non-dimensional distance parameter, x/MS. It is noted that thermocouples have no data for the near hole region of x = 0.

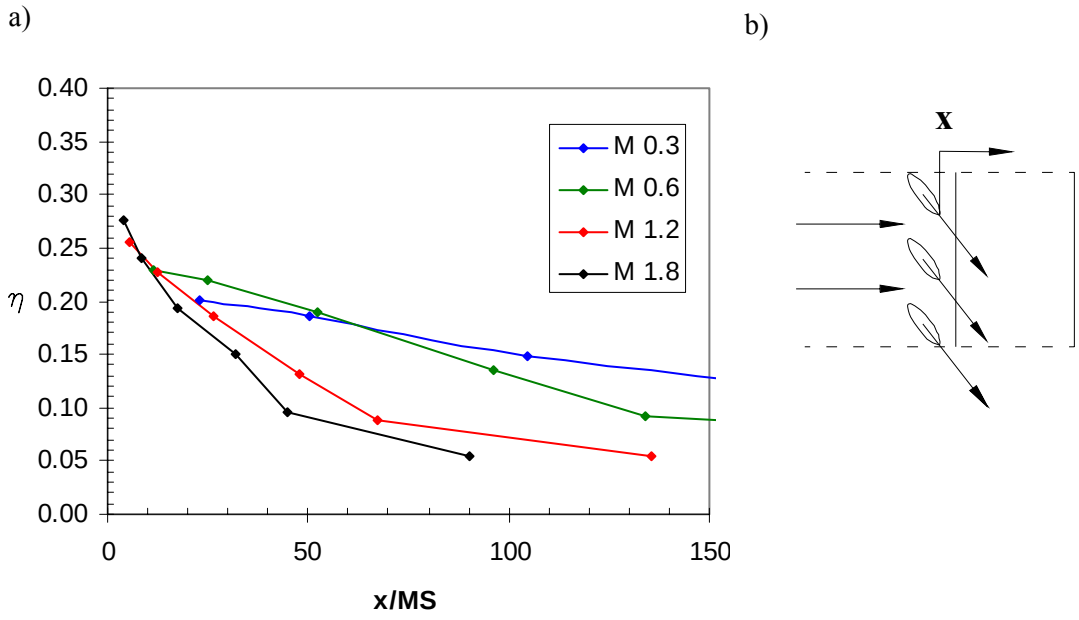

Figure 22. (a) Laterally averaged effectiveness of Plate 1 using the thermocouple method, (b) area of the 3 middle holes of Plate 1 used to average the effectiveness

For the thermocouple measurements, results show the blowing ratio of M = 0.6 to be the optimum blowing ratio since it produces the highest overall effectiveness. Separation and reattachment is not observed by the thermocouples because there were not enough measurement locations to map the trend. All four sets of data do not correlate converge when plotted against the x/MS parameter. However, it seems that the two higher blowing ratios could be correlated together, and the two lower blowing ratios could also be correlated together.

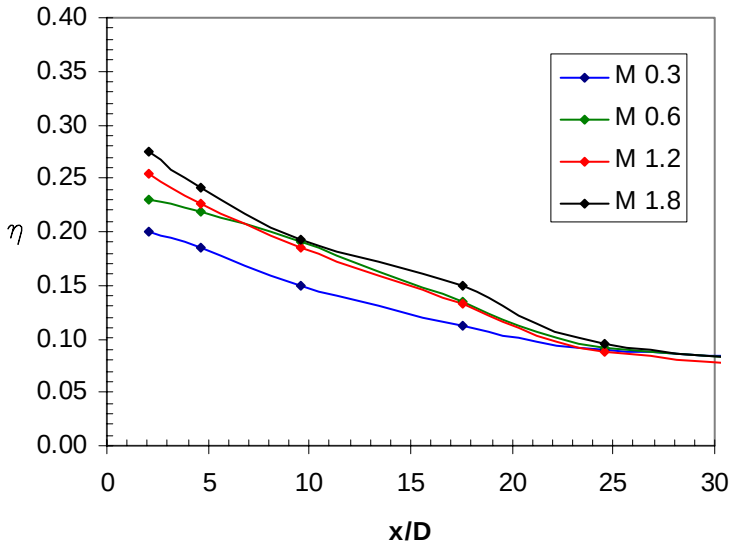

Figure 23. Laterally averaged effectiveness versus the x/D parameter of Plate 1 using the thermocouple method

When looking at the effectiveness plotted versus the x/D parameter, as seen in Figure 23, the highest blowing ratio shows the highest peak effectiveness and the lowest blowing ratio shows the lowest peak effectiveness. All blowing ratios show a decline in effectiveness as x/D increases, and all cases converge at x/D = 25 to an effectiveness level of 0.08.

The uncertainty analysis described in Kline and McClintock [39] was also used for the thermocouple measurements. The thermocouples had a measurement error of ± 0.2ºC The averaged uncertainty of the film effectiveness was found to be ± 8%.

Infrared Thermography

The infrared thermography technique records the surface temperature with a Mikron Thermo Tracer 6T62. The IR-system consists of an optical scanner which directs the incoming infrared radiation line by line onto the detector working in a wavelength

bandwidth of 8 – 13 microns. The output signal is digitized by a processing computer in a frame of 256 x 207 pixels. With the optical zoom, this camera had a depth field of approximately 8.5 x 7 in. when focused on the test surface located 24 in. below the camera. The IR camera viewed the test surface through a sheet of Vinylidene Chloride-Vinyl Chloride co-polymer (Saran Wrap food wrap) which served as an infrared window in the top wall of the wind tunnel. The camera was calibrated with the Saran Wrap in place to account for any bias of the detector sensitivity resulting from minor infrared absorptions. When the window was removed, there were no obstructions between the IR camera and the test surface. Calibrations were preformed by heating a copper plate lined with high emissivity black electrical tape. A foil heater was placed under the 0.635 cm copper plate, and an input voltage was applied to the foil heater so that the surface temperature measurements of the copper plate were taken at increments of 1 - 2ºF. The copper plate was placed on the test surface so that the distance and angle of the IR camera would be identical to that of the test surface. A thermocouple was used to measure the temperature of the copper plate, while the IR camera recorded the temperature of each pixel at every temperature step. An area of 10 x 10 pixels from the IR camera was averaged to get a temperature reading for the copper plate, and this temperature was compared to the reading of the thermocouple. Enough time was allowed between each temperature step so that the copper plate obtained steady state conditions. Figure 24 shows the IR camera calibration with the window in place and without the window in place.

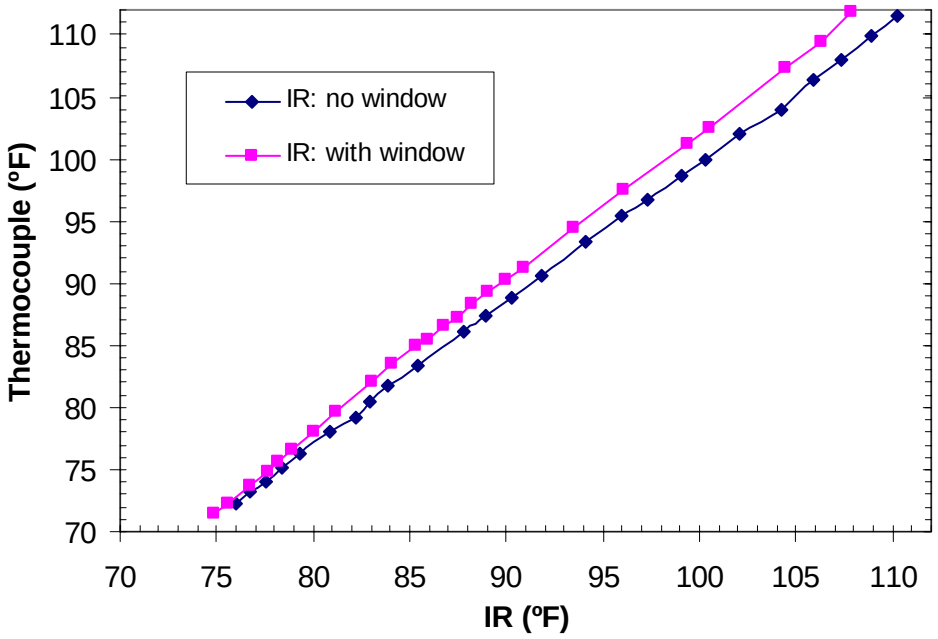

Figure 24. Calibration curve of the IR camera system

The test surface used for the thermocouples method was lined with the same high emissivity black electrical tape used for the calibration procedure, and the downstream edge of the film cooling plate was lined with aluminized thin foil to orientate the infrared camera displays. The coolant air was heated to approximately 40ºC and the mainstream was at room temperature. For each of the four blowing ratios, an image was taken by the IR camera after steady state conditions were reached. These temperatures were written to a computer file and then used to calculate the film cooling effectiveness by using the calibration curve and Equation 2.

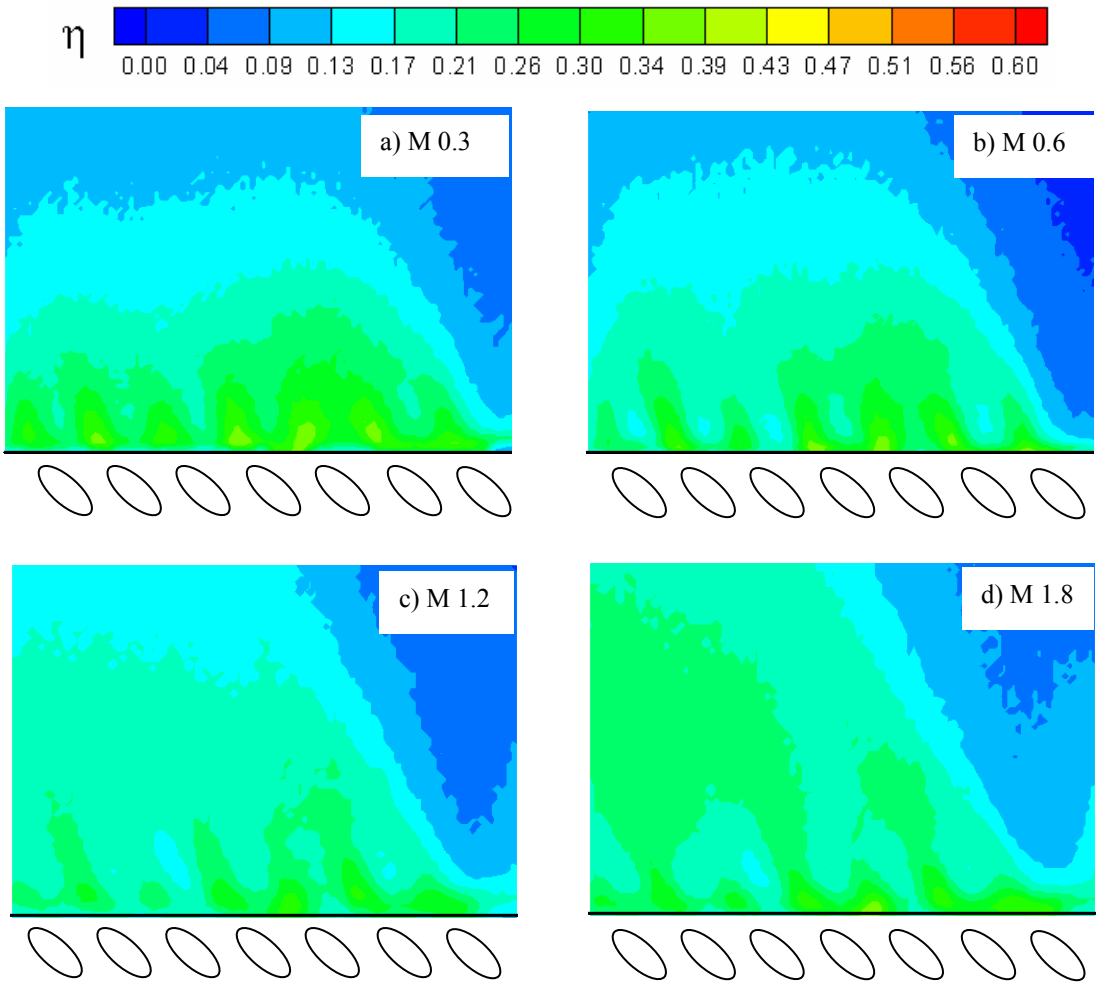

Figure 25. Local effectiveness plots of Plate 1 using the IR method for blowing ratios of (a) 0.3, (b) 0.6, (c) 1.2, and (d) 1.8

Figure 25 shows the local effectiveness results with the IR camera method for all four blowing methods of Plate 1. The black line represents the start of the Plexiglas test surface. Like the other measurement results, the IR method shows that as the blowing ratio increases, the coolant covers more area downstream. The coolant trace can be clearly seen for the three highest blowing ratios. However, for M = 0.3, it seems that the coolant trace from each hole merges together. This is mostly due to the conduction effect at the edge of the Plexiglas test surface. In addition, because of the low coolant momentum at the exit of the holes and the compound angle, the coolant is easily

deflected to the mainstream direction which causes more lateral coverage of the coolant. This is also true for M = 0.6 because this case also shows good lateral coverage. It also shows a higher effectiveness than M = 0.3 in the far downstream region. As the blowing ratio increases to M = 1.2, it is shown that the coolant looses its lateral coverage as the exit momentum increases. However, any coolant separation and reattachment is not visible for this case. Finally, for M = 1.8, the coolant is shown to separate from the surface and then reattach downstream of the holes because of the higher momentum. Although separation is seen for M = 1.8, this case does have the highest effectiveness in the far downstream region.

Figure 26(a) presents the laterally averaged effectiveness of the three middle holes, seen in Figure 26(b), plotted versus the x/MS parameter.

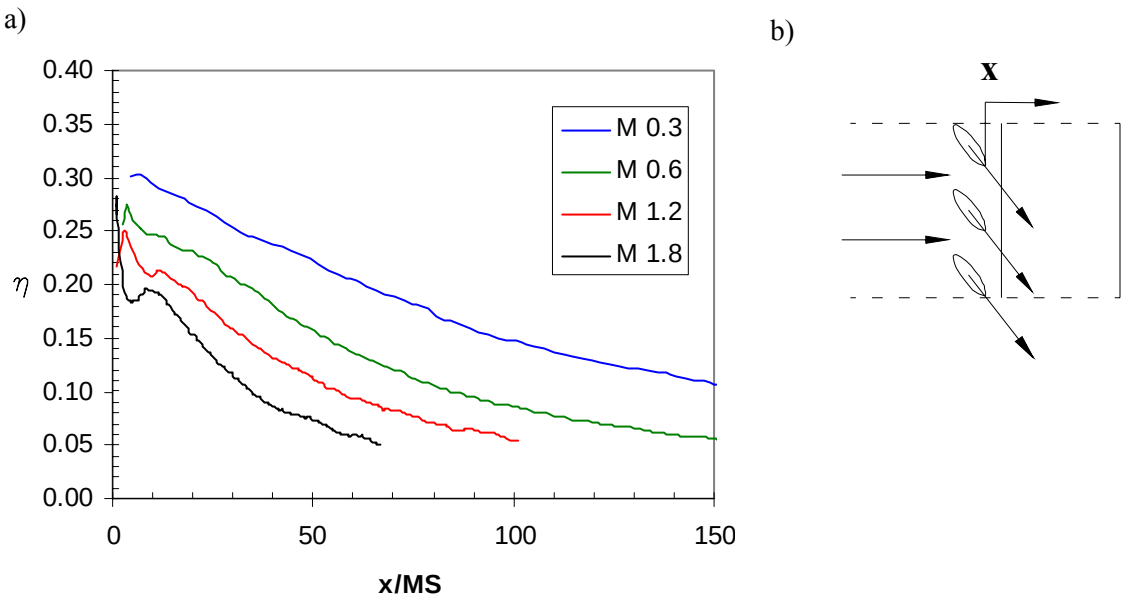

Figure 26. (a) Laterally averaged effectiveness of Plate 1 using the IR method, (b) area of the 3 middle holes of Plate 1 used to average the effectiveness

As the blowing ratio increases, the effectiveness decreases when plotted versus the x/MS parameter. All cases eventually drop to an effectiveness level of 0.05. The separation of

the coolant can be seen for M = 1.8 and minor separation can be seen for M = 1.2. The x/MS parameter, though, does not correlate the data for all four blowing ratios very well.

Figure 27 shows the laterally averaged effectiveness of the three middle holes plotted versus the x/D parameter.

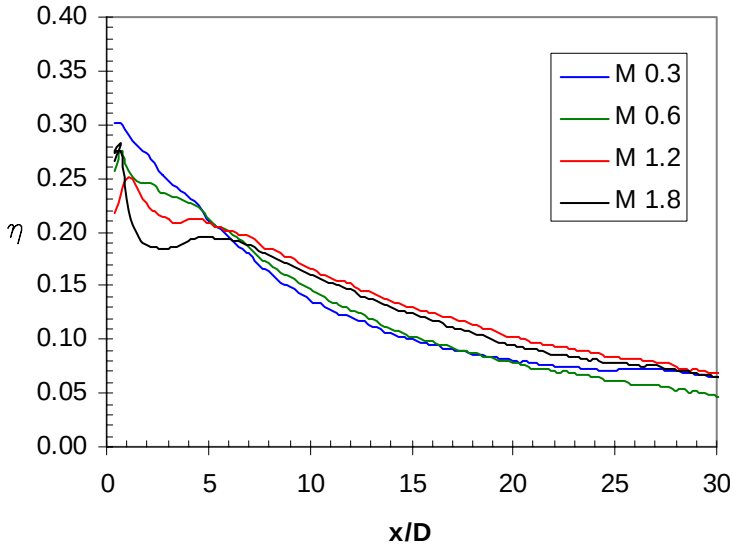

Figure 27. Laterally averaged effectiveness of Plate 1 using the IR method plotted versus x/D

The lowest blowing ratio case of M = 0.3 shows the highest peak effectiveness of 0.3 immediately downstream of the holes. This, however, is due to the conduction of the hot film cooling plate to the upstream edge of the test plate. For M = 0.6, the peak effectiveness is about 0.28, and it has the next highest averaged effectiveness for the region around the holes. The separation for M = 1.2 and 1.8 is seen at x/D = 1, then it reattaches for both cases at x/D = 5. The case for M = 1.2 shows the highest effectiveness for the downstream regions (x/D > 6). Although M = 0.6 should be the optimum blowing ratio, it seems from this figure that M = 1.2 would be the optimum blowing ratio due to the fact that it retains the highest effectiveness for x/D > 6.

The uncertainty of the infrared thermography was calculated by the procedure discussed in Kline and McClintock [39]. The uncertainties of the mainstream (T_m) and coolant (T_c) temperatures were each ± 0.2ºC, and the uncertainty of the surface temperature (T_w) was ± 0.1ºC. The average uncertainty of the effectiveness (η) was estimated at ± 8.8%. Therefore, the accuracy of the measurements was within ± 0.02 effectiveness units for the worst case.

Overall Comparison

Figure 28 plots the average effectiveness of the cylindrical holes for each measurement technique. Each blowing ratio is plotted separately in Figures 28(a-d). Again, the average effectiveness is taken for the span of the three middle holes.

When comparing the different figures, it can be seen that as the blowing ratio increases, the effectiveness plots of each method show less deviation of each other. All methods converge towards the PSP data as the blowing ratio increases. As a result, the conduction effect seems to become greater as the blowing ratio decreases.

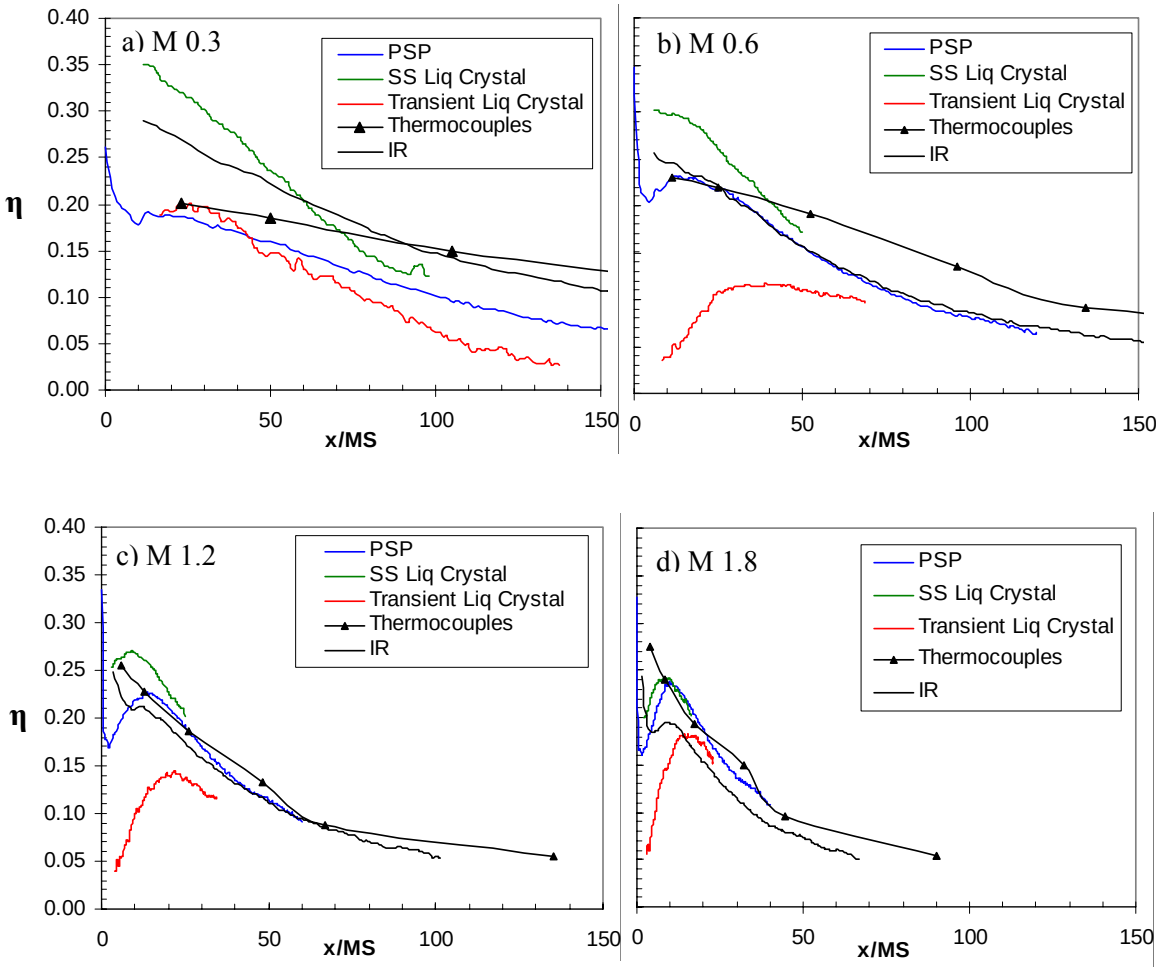

Figure 28. Effectiveness comparison of all measurement methods for Plate 1

Overall, the steady state liquid crystal, PSP, and thermocouple techniques agree with each other, especially for the higher blowing ratios. The transient liquid crystal method always predicted lower effectiveness values than all of the other methods. The location of the peak effectiveness for the PSP and steady state liquid crystal methods agree with each other quite well for the higher blowing ratios. The IR method agreed well with the PSP for the three highest blowing ratios. There were not enough measurement points to determine the peak effectiveness or the separation for the thermocouple method.

Figure 29 compares the effectiveness of the test methods when plotted against the x/D parameter.

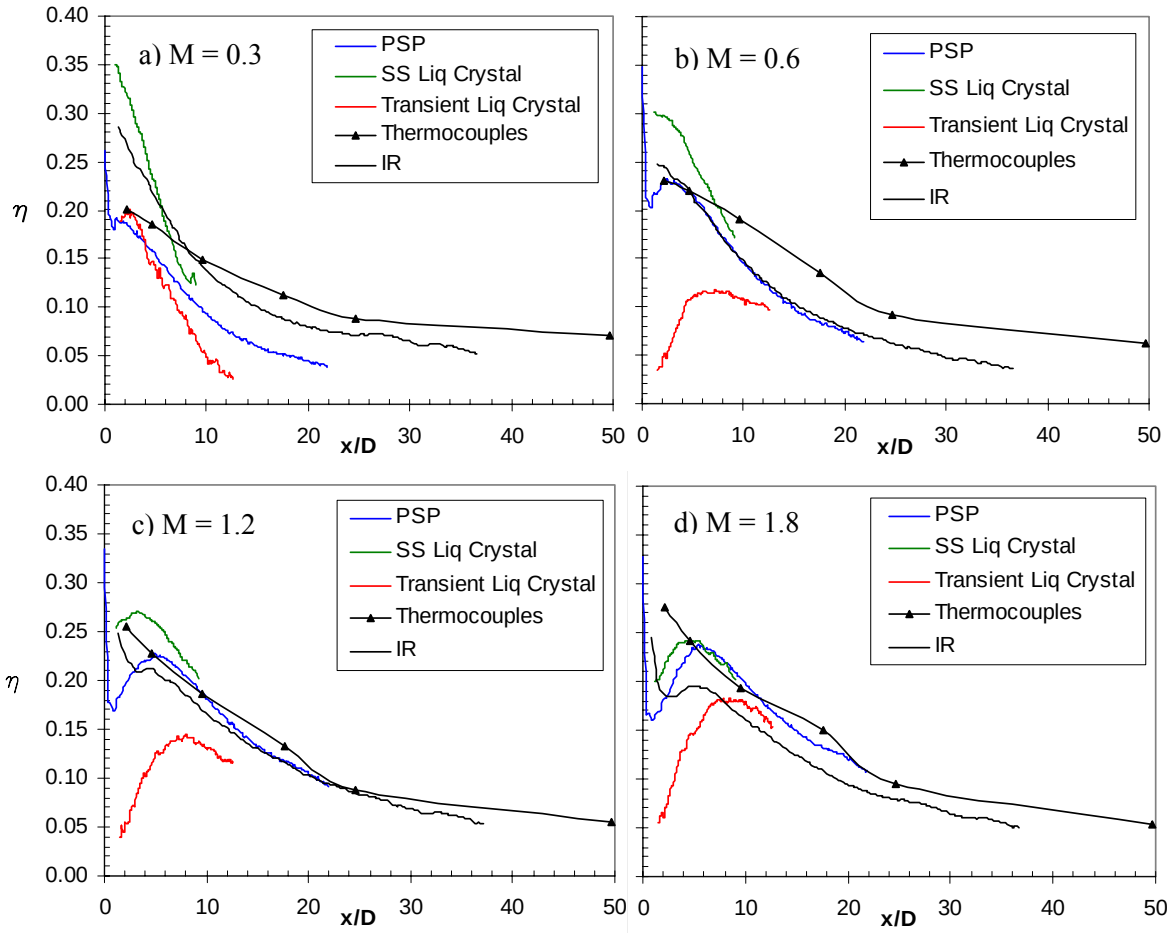

Figure 29. Effectiveness comparison of all measurement methods for Plate 1 plotted versus the x/D parameter

The location of the peak effectiveness is seen to move further downstream as the blowing ratio increases. The most discrepancy between the measuring methods occurs for x/D < 6, which is the location of the maximum conduction effect.

Because all of the data seems to converge towards the PSP data, and because there are no conduction effects in the PSP data, the effectiveness measurements for Part 2 will be

made with the PSP method. Figure 30 compares the PSP results of the cylindrical holes with the compound angle with data taken from open literature for M = 0.6.

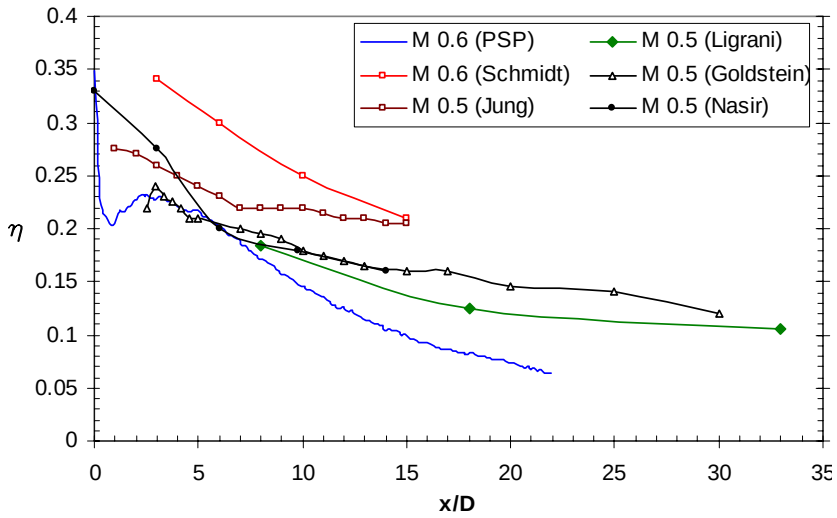

Figure 30. Laterally averaged effectiveness of M = 0.6 measured by the PSP method compared with that measured from other sources.

The PSP data for M = 0.6 is compatible to the other references of M = 0.5. Schmidt et al. [4] used thermocouples and an infrared camera to measure cylindrical holes with θ = 35º and β = 60º. With a hole spacing of 3D and a free-stream turbulence level of 0.2%, Schmidt's data shows the highest averaged effectiveness. Ligrani et al. [40] measured cylindrical holes with θ = 24º, β = 50.5º, a hole spacing of 6D, and a free-stream turbulence level of 0.13%. The geometry used by Nasir et al. [41] was cylindrical holes with θ = 55º, β = 60º, a hole spacing of 3D, and a turbulence level of 11%. They measured the effectiveness with the transient liquid crystal method. Goldstein and Jin [42] used a naphthalene sublimation technique to measure cylindrical holes with θ = 35º, β = 45º, a hole spacing of 3D, and a free-stream turbulence level of 0.54%. Jung and Lee et al. [43] measured the cylindrical holes with θ = 35º and β = 30º with the steady state liquid crystal method. For the blowing ratio of M = 0.6, the PSP data best agrees with Ligrani and Goldstein for x/D < 10.

Figure 31 compares open literature data with the PSP results for M = 1.2. Nasir et al. [41] shows the lowest effectiveness at roughly 0.1, while Schmidt et al. [4] shows the highest effectiveness at roughly 0.25. The coolant separation detected by the PSP results is not shown by the other references. Nasir was the only researcher able to get effectiveness data immediately downstream of the holes. Once again, the data of Ligrani et al. [40] agrees with the PSP data the best. Goldstein and Jin [42] presented data that was also close to the PSP data for x/D < 10. The data of Jung and Lee [43] was higher than the PSP data for M = 0.6 but lower than the PSP data for M = 1.2. The same is true for Nasir et al. [41].

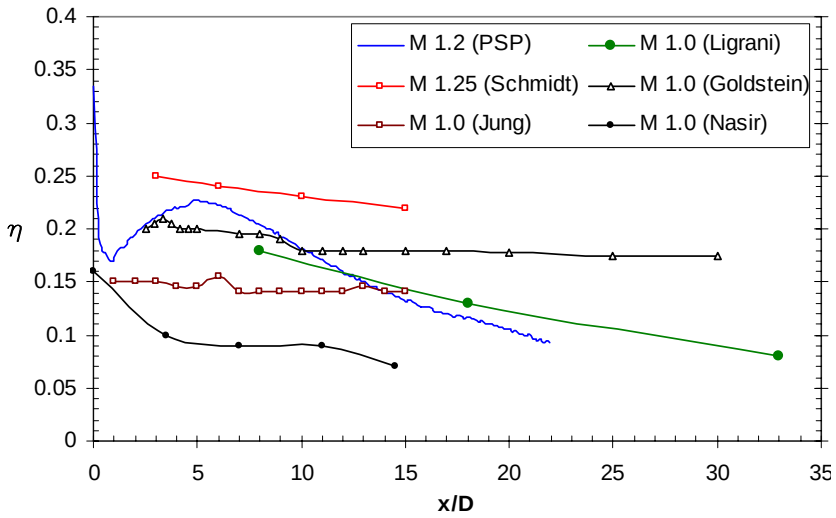

Figure 31. Laterally averaged effectiveness of M = 1.2 measured by the PSP method compared with that measured from other sources.

When comparing the PSP data to the open literature data, especially for M = 0.6, the effectiveness values of the PSP are lower than that of the other sources when x/D > 10. This data is based upon a turbulence level of 6%, whereas the other authors use a turbulence level of 0.54 % or less. Nasir et al. [41] is the only author with a high turbulence level of 11%, and for the high blowing ratio, their data is considerably lower that all of the other data. It has been shown that increasing turbulence levels will

decrease the effectiveness performance. To test this prediction, the infrared camera system was used to retest the effectiveness of Plate 1 and the turbulence grid was removed. As studied in Young et al. [38], the turbulence levels of the wind tunnel with the turbulence grid at the location of the test surface was around 6%. With the turbulence grid removed, however, the turbulence intensity drops to 0.5%. Figure x plots the laterally average effectiveness results of Plate 1 with and without the turbulence grid. For a direct comparison, the data with the grid and without the grid were both measured by the infrared thermography system. The averaged area spans the three middle holes as in the previous plots.

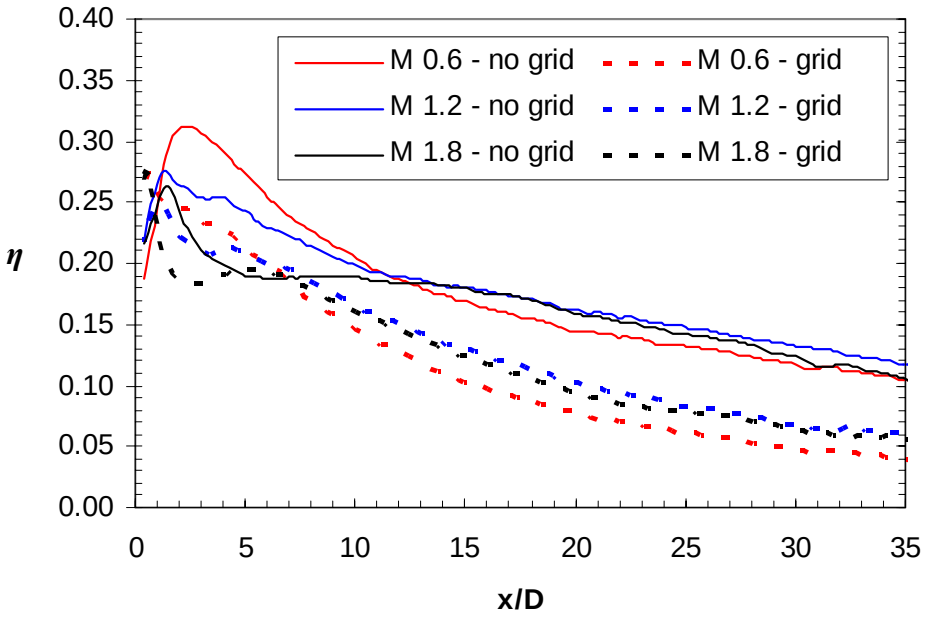

Figure 32. Laterally average effectiveness results for Plate 1 with and without the turbulence grid taken by the IR system

As seen in Figure 32, the lower turbulence levels produce the higher effectiveness levels. The case without the grid shows the higher effectiveness for all x/D locations. The effectiveness for all three blowing ratios at x/D = 35 converges to 0.05 with high turbulence, where as the effectiveness without the grid converges to 0.1. This is an increase of 100%. The peak effectiveness levels are also seen to increase by about 20%

for the case without the turbulence grid, and the blowing ratio of M = 0.6 is still seen to be the optimum blowing ratio.

Part 2: Comparison of Hole Geometries

In this section, the effectiveness results for five different film cooling hole geometries are presented. Effectiveness measurements were calculated by the PSP method to eliminate the heat loss factors.

Plate 1

Figure 33 shows the contour plots of the local effectiveness levels for cylindrical holes with a compound angle (Plate 1), which was also calculated for the results of Part 1. As discussed earlier, it can be seen from Figure 33 that as the blowing ratio increases, the trace of the coolant extends further downstream. For M = 0.6, the coolant exiting the holes has the most uniform lateral coverage. As the blowing ratio increases to 1.2 and 1.8, the region immediately downstream of the holes decreases in effectiveness due to the increased coolant momentum. The trace left from the coolant becomes narrower resulting in less coverage and lower effectiveness. This is due to the increase of momentum as the blowing ratio increases. Higher momentum promotes more mixing between the mainstream and coolant flows. The coolant detaches from the surface immediately downstream of the holes exposing the surface to the mainstream flow and decreasing the effectiveness. As the coolant is separated from the surface, it is also pushed by the mainstream flow back to the surface. This reattachment back to the surface results in higher local effectiveness as the coolant impinges back onto the surface. This reattachment can be seen for M = 1.8, where the effectiveness suddenly increases approximately 7 diameters downstream of the holes. The reattachment is less for M=1.2, and it occurs approximately 5 diameters downstream.

It is also noted that the region inside of the holes for the three highest blowing ratios has effectiveness levels in the range of 0.95 to 0.99, which is expected. However, for M = 0.3, the effectiveness level is only around 0.7.

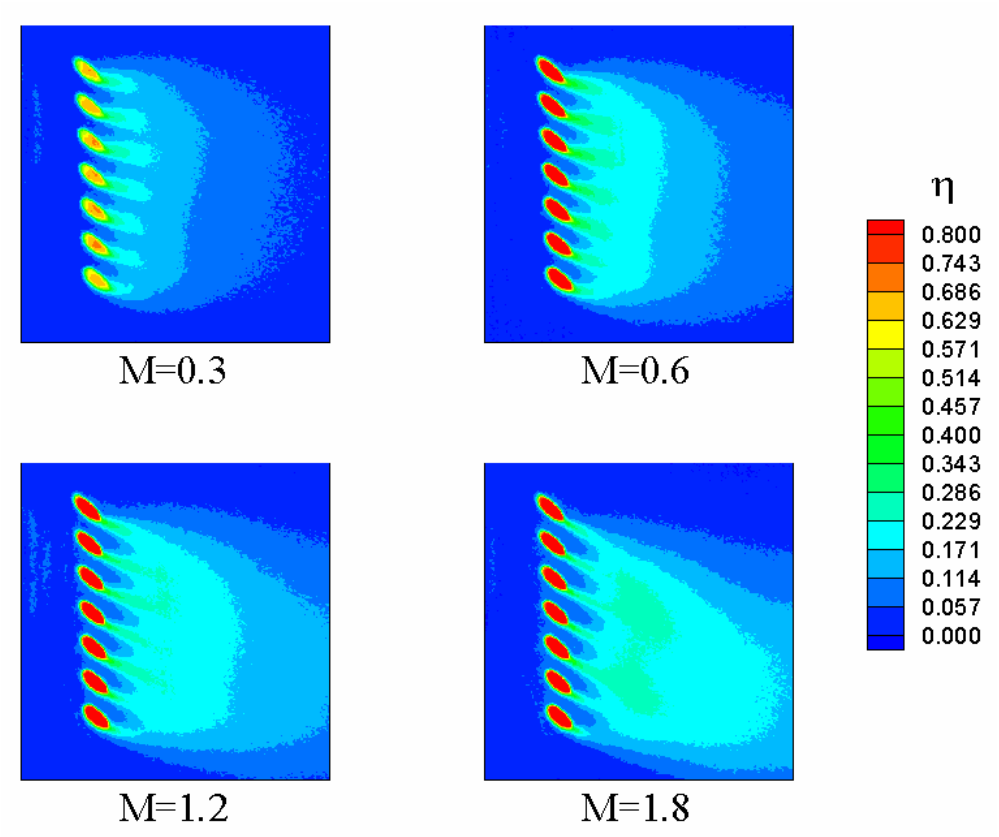

Figure 33. Local effectiveness plots of Plate 1 using PSP for blowing ratios of (a) 0.3, (b) 0.6, (c) 1.2, and (d) 1.8

Figure 34 shows the laterally averaged effectiveness for the three middle holes at each blowing ratio plotted versus the x/D parameter. The downstream area that was averaged for the three middle holes (holes # 3, 4, and 5) is also shown in Figure 34. It spans from the outermost edge of the third hole to the outermost edge of the fifth hole. Averaging the effectiveness shows that M = 0.6 has the highest effectiveness for the region nearest to the holes. Separation and reattachment is strongly seen for M = 1.8 and 1.2 as the effectiveness immediately decreases but then increases to a maximum, or peak effectiveness. The highest blowing ratio of M = 1.8 has the highest effectiveness in the

far downstream region, but the lowest effectiveness at the exit of the holes. The lowest blowing ratio has the lowest peak effectiveness and the lowest effectiveness for x/D > 2.

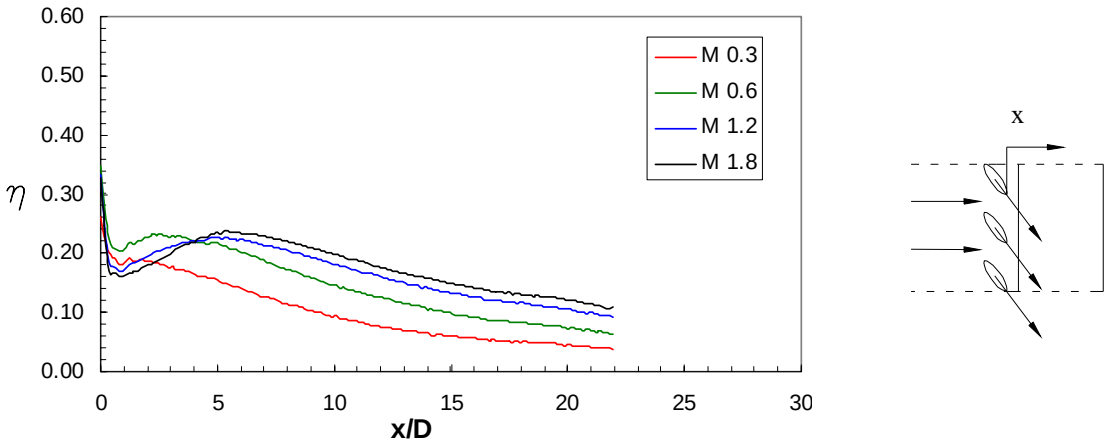

Figure 34. Laterally averaged effectiveness for the three middle holes of Plate 1 plotted versus the x/D parameter

Figure 35 shows the effectiveness plotted versus the x/MS parameter.

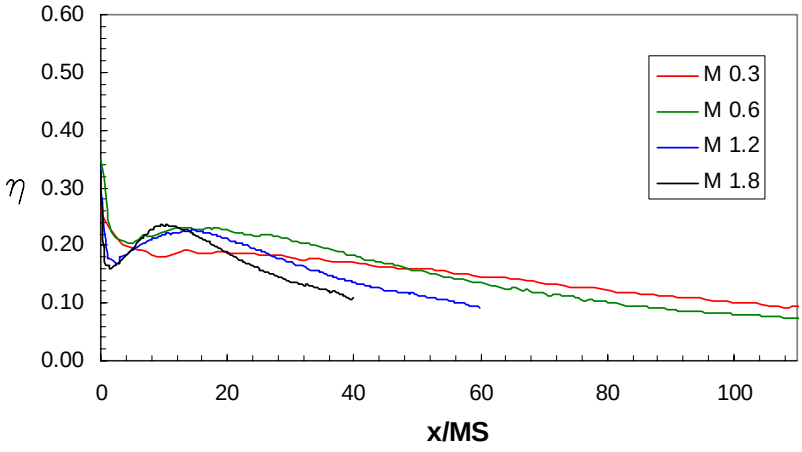

Figure 35. Laterally averaged effectiveness for the three middle holes of Plate 1 plotted versus the x/MS parameter

Plotting the effectiveness versus the x/MS parameter shows that the data for all four blowing ratios does not fall onto one correlation curve. The three highest blowing ratios seem to follow the same trend, whereas the lowest blowing ratio of M = 0.3 shows a different trend.

Plate 2

Figure 36 shows the local effectiveness for the fan-shaped laidback holes with the axial angle (Plate 2).

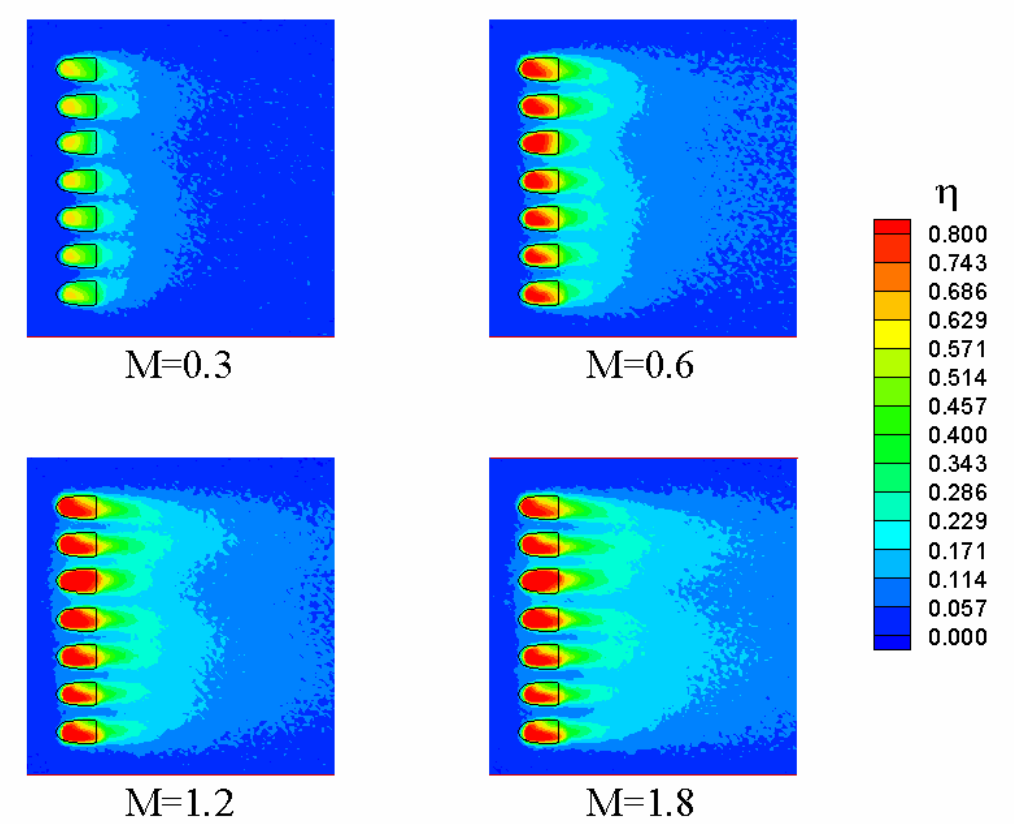

Figure 36. Local effectiveness plots of Plate 2 using PSP for blowing ratios of (a) 0.3, (b) 0.6, (c) 1.2, and (d) 1.8

The lateral expansion of the holes provides an all around more uniform lateral coverage of the downstream surface. Because there is only an axial angle for this geometry,

changing the blowing ratio does not affect the lateral trace of the coolant because there is no lateral momentum in the coolant. In other words, the width of the coolant trace is the same for every blowing ratio. The 10-degree lateral expansion produces a fairly uniform coverage, except for a small area of low effectiveness between each hole. The only difference between the blowing ratios is the coverage length of the coolant trace. As the blowing ratio increases, the effectiveness coverage expands further downstream. There is no separation and reattachment seen for this geometry due to the 10-degree streamwise expansion of the holes. The increased exit area of the hole decreases the coolant momentum enough to keep the coolant attached to the surface, even for M = 1.8. The effectiveness inside the hole region is not uniform for any of the blowing ratios. The effectiveness levels inside the hole range from 0.97 down to 0.50 on the expanded corners of the hole. This suggest that the coolant momentum is reduced enough to allow the mainstream to partially enter the exit hole area. For M = 0.3, the effectiveness level inside the holes ranges from 0.65 to 0.40.

Looking at the averaged effectiveness of the three middle holes seen in Figure 37, the blowing ratio of M = 1.8 and 1.2 have the highest effectiveness immediately downstream of the holes. The averaged area spans from the outer edge of the third hole to the outer edge of the fifth hole, as seen in Figure 37. In addition, M = 1.8 has the highest effectiveness far downstream of the holes. The trend for the axial fan-shaped laidback holes shows that as the blowing ratio increases, the effectiveness increases. It should be noted, though, that increasing the blowing ratio from M = 1.2 to 1.8 does not increase the peak effectiveness. The peak effectiveness for Plate 2 occurs immediately downstream of the holes, unlike that of the cylindrical holes.

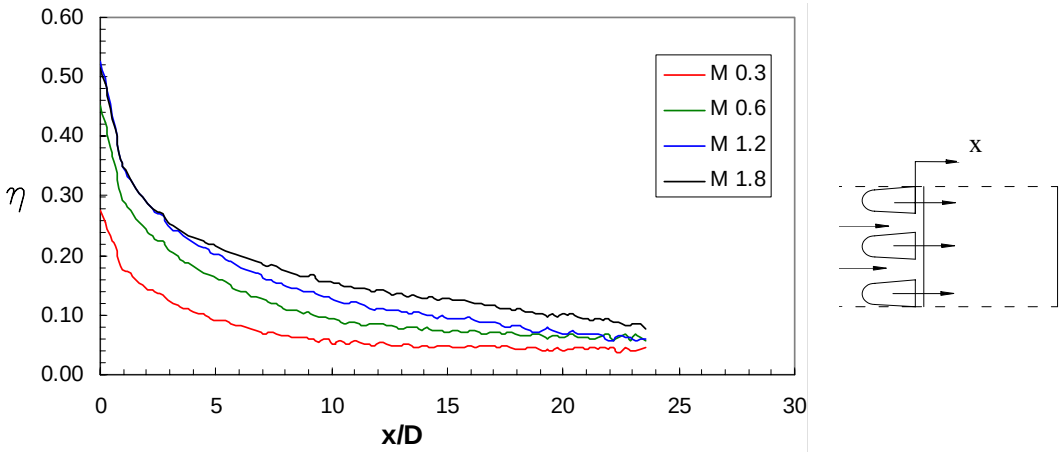

Figure 37. Laterally averaged effectiveness for the three middle holes of Plate 2 plotted versus the x/D parameter

Figure 38 shows the averaged effectiveness plotted versus the x/MS parameter.

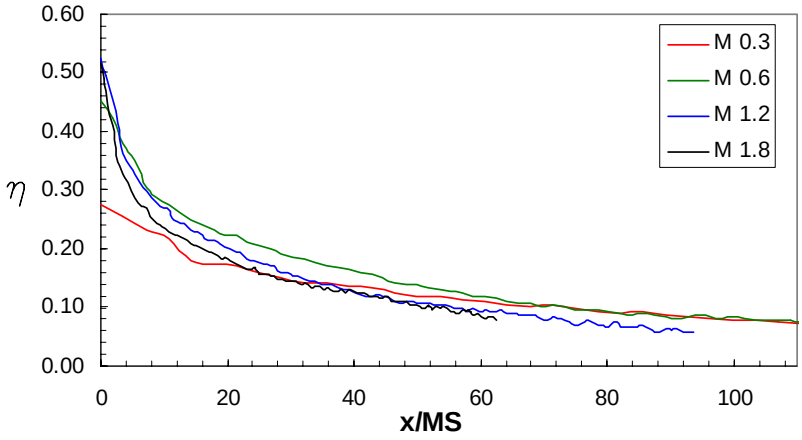

Figure 38. Laterally averaged effectiveness for the three middle holes of Plate 2 plotted versus the x/MS parameter

These effectiveness plots for Plate 2 are able to be correlated better than those of the cylindrical holes. Each blowing ratio is within 10-15% of the other cases. A single correlated curve would represent the effectiveness data for Plate 2 much better that a single correlated curve for Plate 1.

Plate 3

Figure 39 shows the local effectiveness contours for the fan-shaped laidback holes with a compound angle (Plate 3).

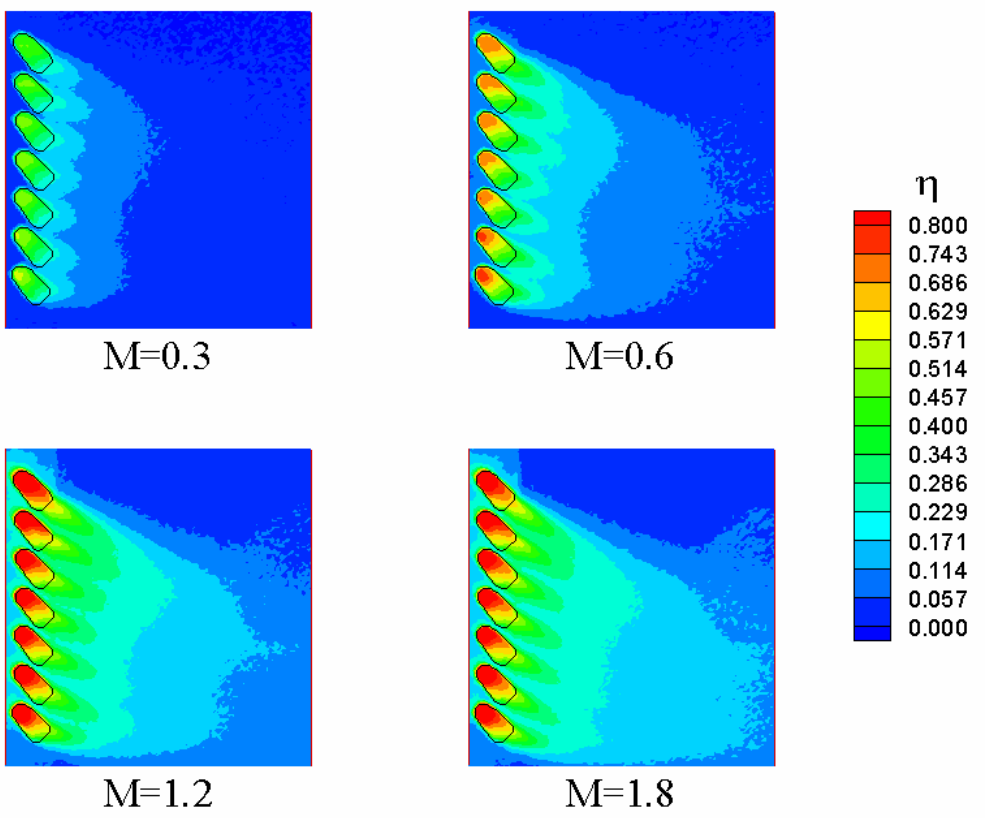

Figure 39. Local effectiveness plots of Plate 3 using PSP for blowing ratios of (a) 0.3, (b) 0.6, (c) 1.2, and (d) 1.8

For the compound angled fan-shaped laidback holes, M = 1.2 seems to provide the most uniform coverage in the lateral direction. The gaps between the holes are well covered due to the lateral expansion of the holes and the compound angle, which increases the lateral momentum of the coolant. The effectiveness levels for M = 1.2 and M = 1.8 do not seem to vary much, except that M = 1.8 has higher coverage in the far downstream regions. No separation or reattachment is noted for any of the blowing ratios. This is

due to the expanded exit areas decreasing the coolant momentum. The regions inside the holes for M = 1.2 and 1.8 have an effectiveness ranging from 0.95 to 0.60. Whereas M = 0.6 has effectiveness levels ranging from 0.75 to 0.40, and M = 0.3 ranges from 0.50 to 0.30.

Figure 40 shows the laterally averaged effectiveness for the three middle holes of Plate 3. The averaged area of Plate 3 is also defined in Figure 40. It spans from the outermost edge of the third hole to the outermost edge of the fifth hole. The blowing ratios of M = 1.2 and 1.8 are very similar, with M = 1.8 having a small increase of effectiveness at the far downstream regions. The lowest blowing ratio has the smallest effectiveness levels. The trend for the compound angle fan-shaped laidback holes seems to have an increasing effectiveness with an increasing blowing ratio up to M = 1.2.

The peak effectiveness for Plate 3 occurs immediately downstream of the holes (x/D < 1). The two highest blowing ratios have the highest peak effectiveness of 0.4, while the lowest blowing ratio has the lowest peak effectiveness of 0.2. It also has the lowest effectiveness for all x/D.

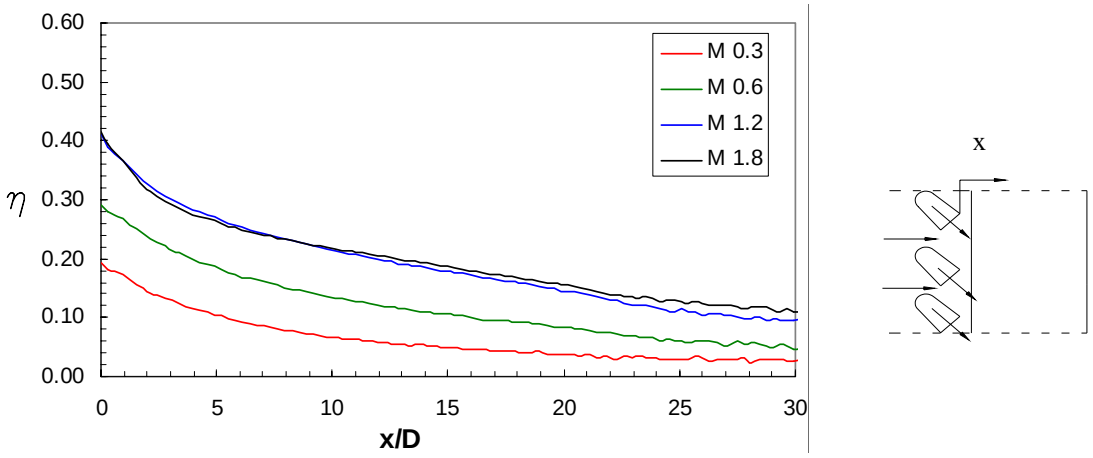

Figure 40. Laterally averaged effectiveness for the three middle holes of Plate 3 plotted versus the x/D parameter

Figure 41 shows the effectiveness plotted versus the x/MS parameter.

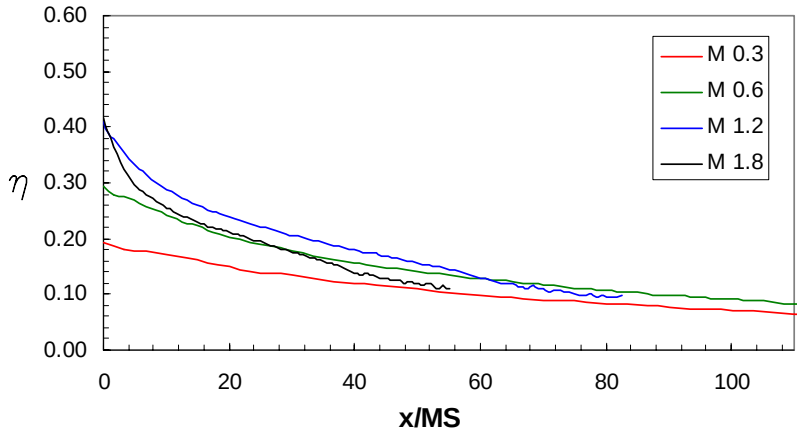

Figure 41. Laterally averaged effectiveness for the three middle holes of Plate 3 plotted versus the x/MS parameter

The data from Plate 3 does not correlate as well as that of Plate 2. There is approximately 30% difference between the highest and lowest blowing ratios.

Plate 4

Figure 42 shows the local effectiveness plots for the conical shaped holes with an axial angle (Plate 4). As seen from the figure, the overall levels of effectiveness are much lower compared to the previous hole geometries. The optimum blowing ratio seems to be at M = 1.2, as the coolant trace for this case seems to extend farthest downstream. Effectiveness levels inside the holes are 0.95 – 0.97 for the two highest blowing ratios, 0.80 for M = 0.6, and 0.60 for M = 0.3. Due to the axial angle of the holes, the lateral coverage performance is not very good. There is a large area between the holes with low effectiveness at all downstream locations. For M = 1.8, some reattachment is seen at 10 diameters downstream of the holes.

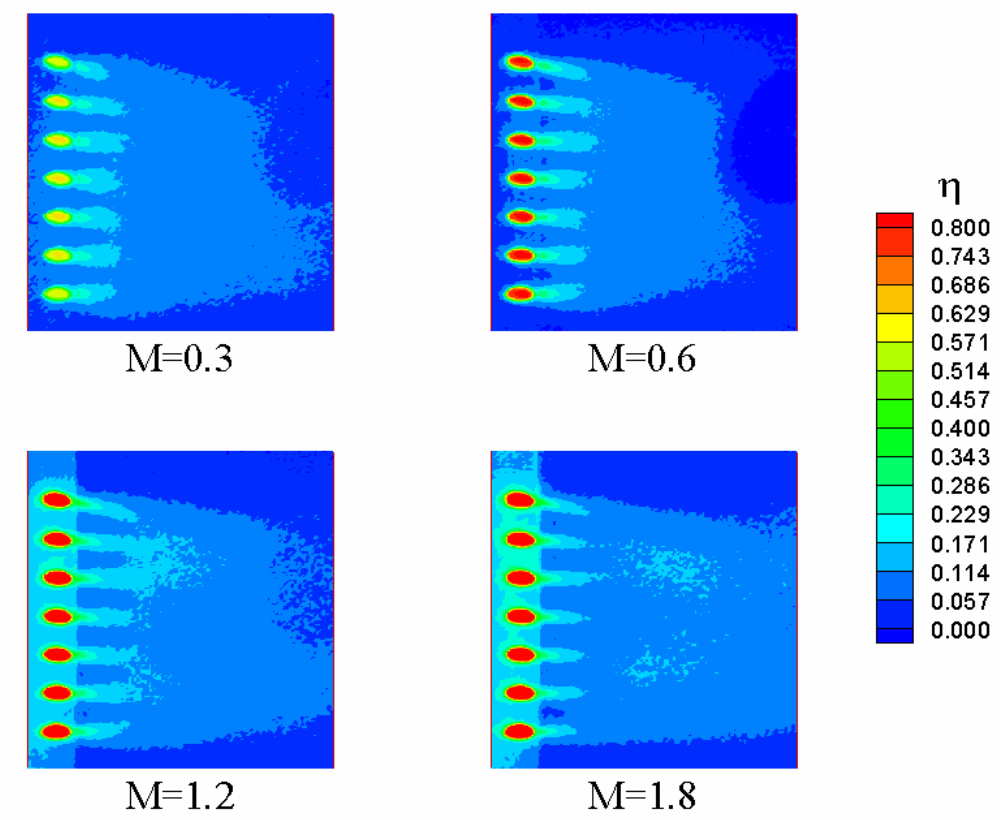

Figure 42. Local effectiveness plots of Plate 4 using PSP for blowing ratios of (a) 0.3, (b) 0.6, (c) 1.2, and (d) 1.8

As seen from Figure 43, the averaged effectiveness of the three middle holes is much lower for the conical shaped holes. The averaged area spans from the outer edge of the third hole to the outer edge of the fifth hole. For the region immediately downstream of the holes, M = 1.2 has the highest effectiveness up to 8 hole diameters. After that, M = 1.8 has the highest effectiveness due to the reattachment of the coolant. The two lowest blowing ratios have nearly identical effectiveness levels for all downstream locations. The highest blowing ratio of M = 1.8 has a peak effectiveness around 0.28 at the exit of the hole. However, because of the separation, it decreases to 0.12 at x/D = 4 and then increases back to 0.15 at x/D = 10.

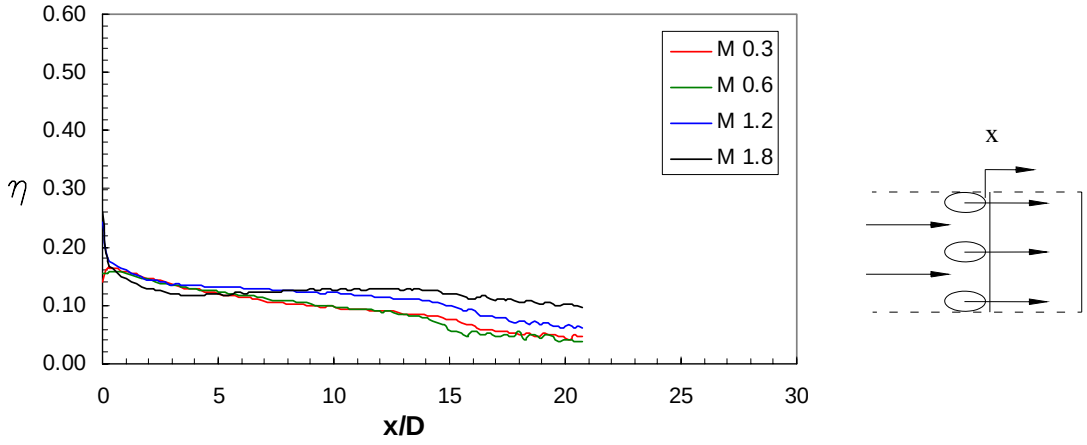

Figure 43. Laterally averaged effectiveness for the three middle holes of Plate 4 plotted versus the x/D parameter

Figure 44 shows the averaged effectiveness plotted versus the x/MS parameter.

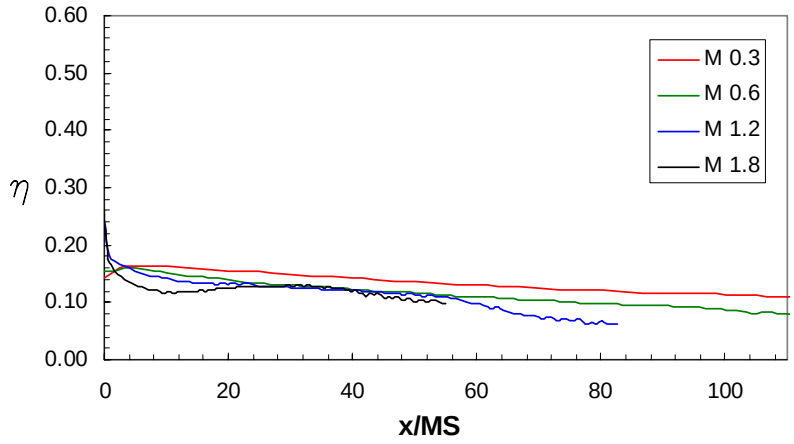

Figure 44. Laterally averaged effectiveness for the three middle holes of Plate 4 plotted versus the x/MS parameter

The data for all four blowing ratios do not correlated well. However, it seems that the data for the two higher blowing ratios could correlate with each other, and the data for the two lower blowing ratios could correlate with each other.

Plate 5

Figure 45 displays the local effectiveness contours for the conical holes with a compound angle.

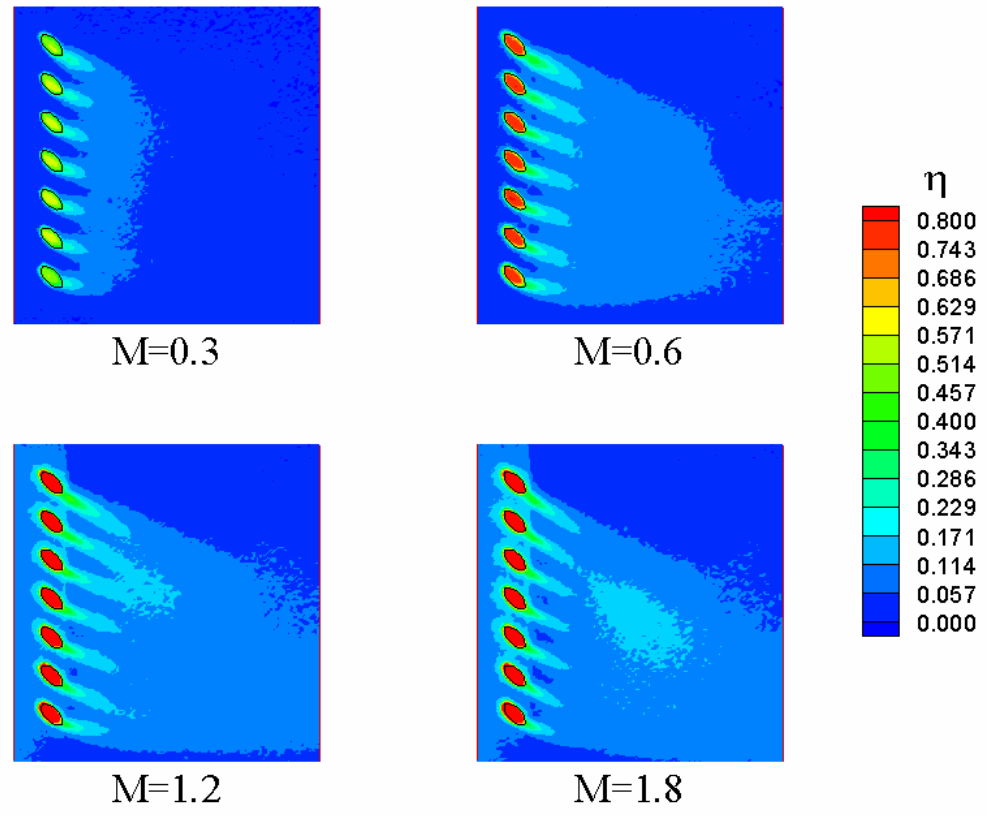

Figure 45. Local effectiveness plots of Plate 5 using PSP for blowing ratios of (a) 0.3, (b) 0.6, (c) 1.2, and (d) 1.8

Like the conical holes with an axial angle, the blowing ratio of M = 1.2 is the optimum blowing ratio. Due to the compound angle, the lateral coverage is a little better than the conical holes with the axial angle. The effectiveness levels inside the holes are 0.95 – 0.96 for the two highest blowing ratios, 0.79 – 0.80 for M = 0.6, and 0.53 – 0.56 for M = 0.3. Reattachment is seen clearly for the blowing ratio of M = 1.8.

Figure 46 shows the laterally averaged effectiveness for the three middle holes of Plate 5. The averaged area, also seen in Figure 46, spans from the outer point of the third hole to the outer point of the fifth hole.

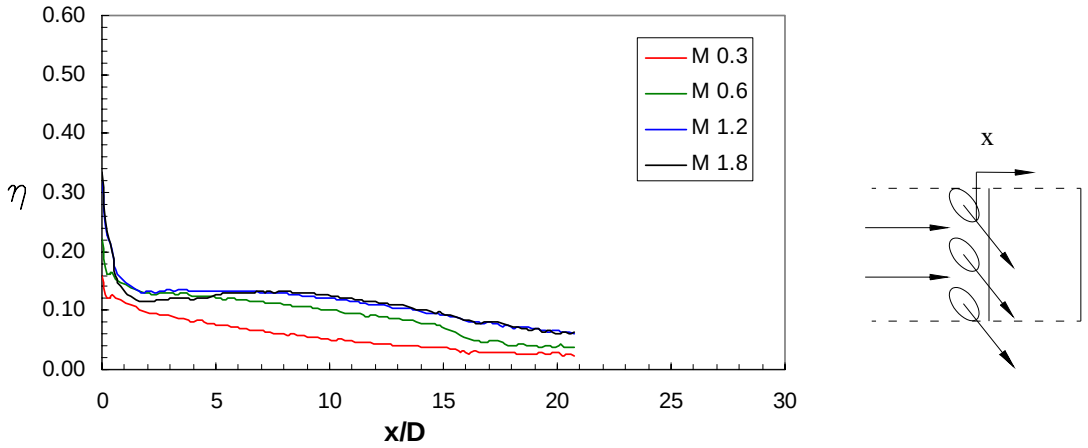

Figure 46. Laterally averaged effectiveness for the three middle holes of Plate 5 plotted versus the x/D parameter

The optimum blowing ratio for the region near the holes is M = 1.2. This case has the highest effectiveness up to 5 hole diameters downstream. After 5 hole diameters, the highest blowing ratio has the highest effectiveness due to reattachment. The lowest blowing ratio of M = 0.3 shows the lowest effectiveness at all downstream locations with a peak effectiveness of 0.14. The peak effectiveness for the two highest blowing ratios is both around 0.23.

Figure 47 shows the averaged effectiveness plotted versus the x/MS parameter.

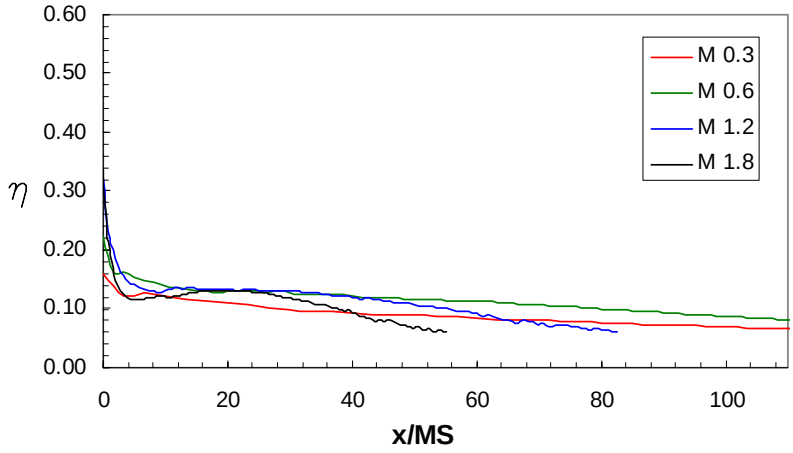

Figure 47. Laterally averaged effectiveness for the three middle holes of Plate 5 plotted versus the x/MS parameter

All peak effectiveness locations are immediately downstream of the holes. Because results for the conical holes (Plates 4 and 5) seemed so low, the author repeated the tests for Plate 5 with the thermocouple method to double check the results. Figure 48 shows the plots of the laterally averaged effectiveness for the thermocouples and PSP measurements plotted versus the x/MS parameter.

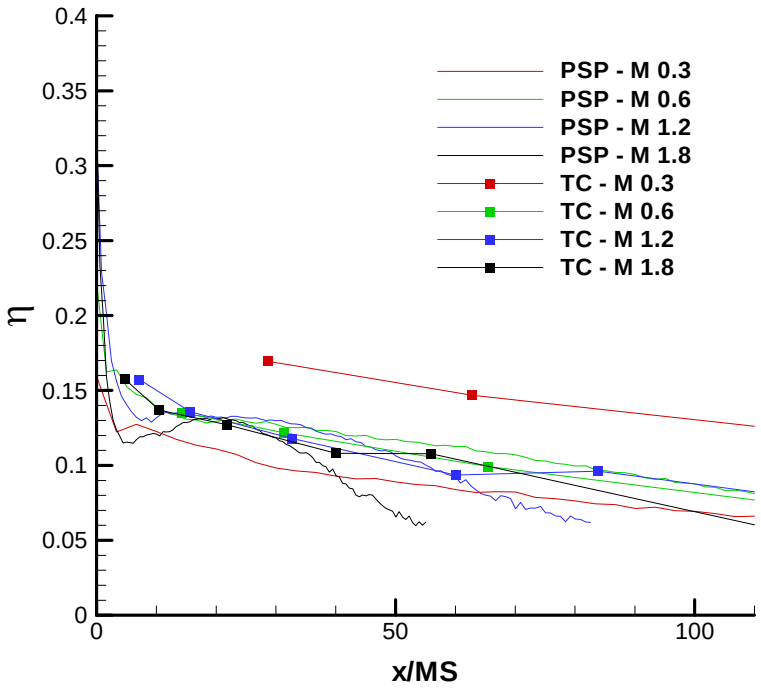

Figure 48. Comparison of the PSP and Thermocouple laterally averaged effectiveness measurements for the three middle holes of Plate 5

The PSP and thermocouple measurements agree well with each other except for the lowest blowing ratio of M = 0.3. This is due to the conduction effects as described earlier.

Overall Comparison

Hole geometries seem to have little effect on film cooling effectiveness when low blowing rates are applied, as seen in Figure 49. All of the plates show roughly the same effectiveness levels and trends.

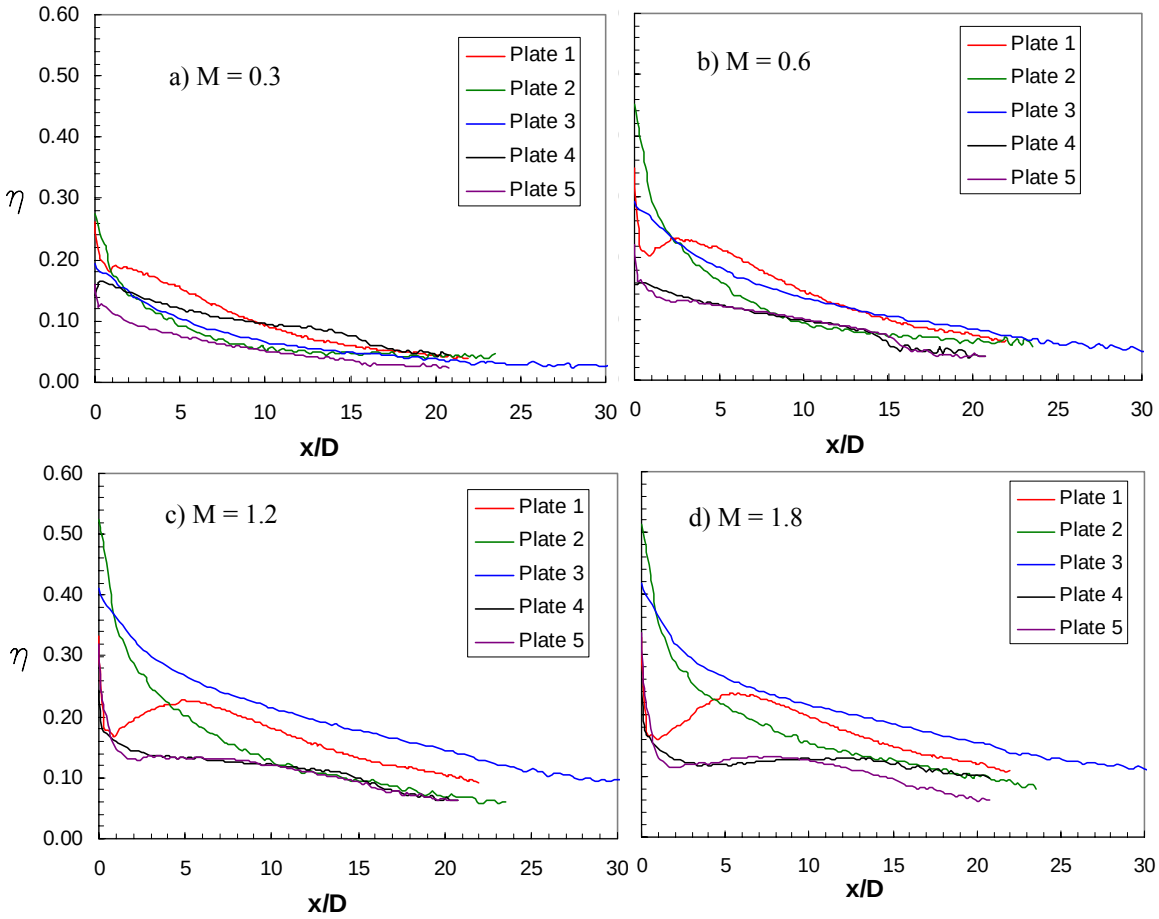

Figure 49. Effectiveness comparison of Plates 1 - 5 plotted versus the x/D parameter

For the blowing ratio of M = 0.6, the Plate 2 shows the highest peak effectiveness at the near hole region. However, the cylindrical holes (Plate 1) have the highest effectiveness for x/D > 4. As the blowing ratio increases to M = 1.2 and M = 1.8, though, the fan-shaped holes (Plates 2 and 3) show the highest effectiveness for all x/D positions. The fan-shaped holes with the axial angle show the highest peak effectiveness at x/D = 0, but as x/D increases, the fan-shaped holes with the compound angle show the highest effectiveness. The conical shaped holes show the lowest effectiveness for all blowing ratios, and there is not much difference between the conical holes with the axial angle and the conical holes with the compound angle. At higher blowing ratios, it is

advantageous to decrease the coolant momentum exiting the holes, which is the design of the fan-shaped holes. However, at low blowing ratios, decreasing the coolant momentum is not advantageous because it lowers the effectiveness below that of the cylindrical holes.

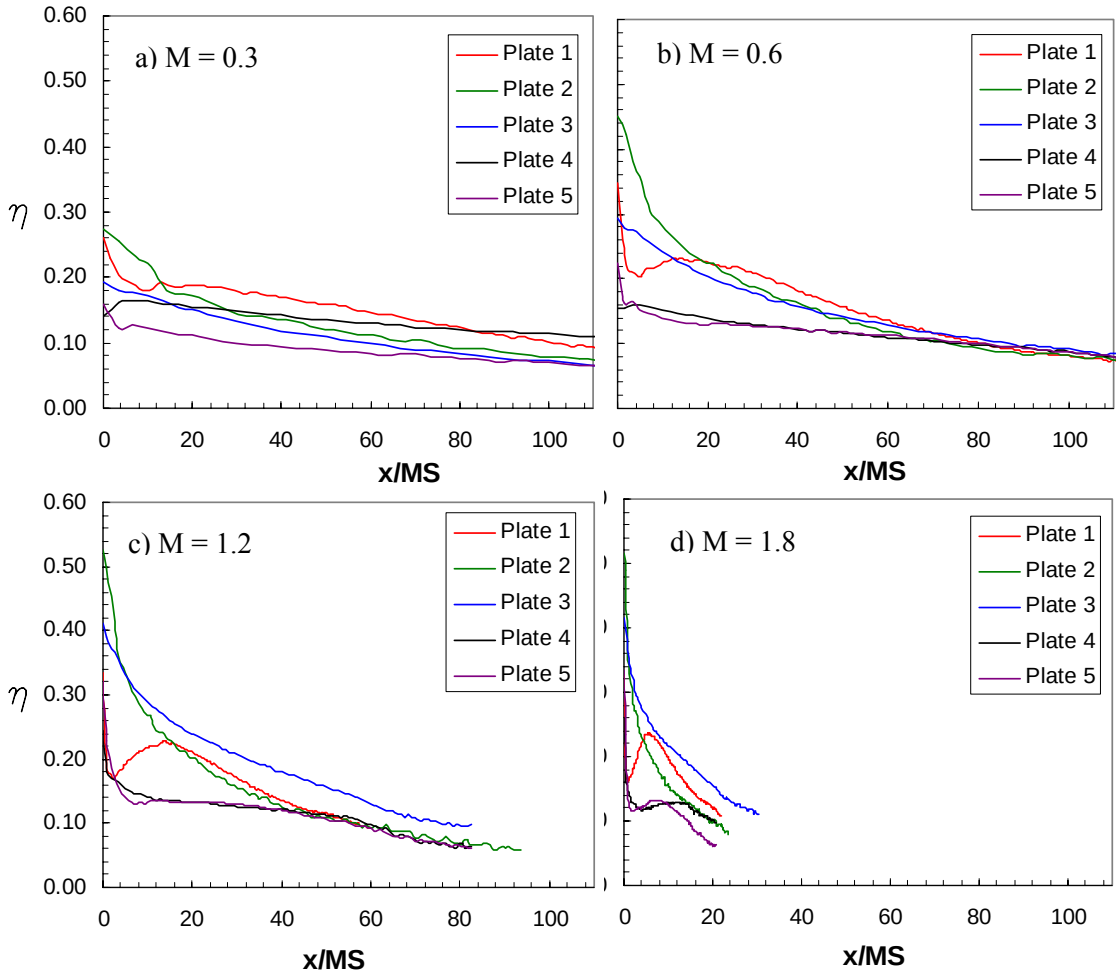

Figure 50. Effectiveness comparison of Plates 1 - 5 plotted versus the x/MS parameter

Figure 50 compares the laterally average effectiveness of the plates versus the x/MS parameter. When comparing the different geometries, it seems that the lowest blowing ratio can reasonably provide a single correlation curve to fit the data for every hole

geometry. The other blowing ratios show a great amount of deviation between the different geometries for x/MS < 50. However, for x/MS > 50, the data converges to effectiveness around 0.1.

CONCLUSIONS

An experimental study has been performed to investigate the film cooling effectiveness measurements of four different techniques: steady state liquid crystal, transient liquid crystal, pressure sensitive paint, and thermocouples. The study then focused on the film cooling performance of various shaped film cooling holes in comparison to the reference geometry of cylindrical holes with a compound angle. The key findings are summarized below.

For Part 1 of the investigation, all methods except for the transient liquid crystal showed the same effectiveness data for the higher blowing ratios. The conduction effect for the three steady state methods (steady state liquid crystal, thermocouples, and infrared thermography) causes a higher percent error in the effectiveness measurements of the lower blowing ratio cases. As a result, the steady state liquid crystal, the thermocouples, and the IR methods yielded higher effectiveness data than the PSP or transient liquid crystal methods. The transient liquid crystal method yielded the lowest effectiveness results for all four blowing ratios, and it had the highest uncertainty. The PSP method is the most precise method for measuring film cooling effectiveness because it eliminates the conduction effects and is able to make accurate measurements around sharp corners and edges.

In Part 2 of the experiment, the PSP method was implemented to measure the effectiveness for all hole configurations. It was found that all configurations showed similar film cooling effectiveness at the lowest blowing ratio of M = 0.3. Shaped holes do not enhance the effectiveness because the momentum of the coolant is too low. For M = 0.6, the two fan-shaped laidback holes showed the highest effectiveness immediately downstream of the holes. The expanded geometries decreased the coolant momentum so that coolant remained on the test surface. However, as x/D increased to a value of 10 or so, the effectiveness of the cylindrical holes surpassed that of the fan-

shaped holes. Shaped holes perform better for higher blowing ratios because they are designed decrease the coolant momentum. If the coolant momentum is already low, as in the case of M = 0.3 and 0.6, then the effectiveness will sharply decline as x/D increases. The effectiveness of the cylindrical holes remained the highest in the downstream locations for M = 0.6 because that is near the optimum blowing ratio for cylindrical holes.

For the higher blowing ratios, the fan-shaped laidback holes performed the best, especially for the regions immediately downstream of the holes. It was shown that of the two fan-shaped holes, the one with a compound angle yielded the highest effectiveness for the downstream locations. Compound angles increase the lateral momentum of the coolant which provides better coverage in the spanwise direction. The conical shaped holes had the worst effectiveness performance, even lower that that of the cylindrical holes. This could be due to the streamwise expansion of the hole in the upstream direction which decreases the coolant momentum even more. It can also be concluded that the degree of expansion in the holes can affect the effectiveness performance.

REFERENCES

[1] Han, J.C., Dutta, S., and Ekkad, S., 2000, *Gas Turbine Heat Transfer and Cooling Technology*, Taylor and Francis, New York, pp. 540-559.

[2] Goldstein, R.J., Eckert, E.G., and Burggraf, R., 1974, "Effects of Hole Geometry and Density on Three Dimensional Film Cooling," Int. J. of Heat and Mass Transfer, **17**, pp. 595–606.

[3] Sen, B., Schmidt, D.L., and Bogard, D.G., 1996, "Film Cooling with Compound Angle Holes: Heat Transfer," ASME J. Turbomachinery, **118**, pp. 800–806.

[4] Schmidt, D.L., Sen, B., and Bogard, D.G., 1996, "Film Cooling with Compound Angle Holes: Adiabatic Effectiveness," ASME J. Turbomachinery, **118**, pp. 807–813.

[5] Thole, K., Gritsch, M., Schulz, A., and Wittig, S., 1998, "Flowfield Measurements for Film Cooling Holes with Expanded Exits," ASME J. Turbomachinery, **120**, pp. 327–336.

[6] Hyams, D.G., and Leylek, J.H., 1997, "A Detailed Analysis of Film Cooling Physics Part III: Streamwise Injection with Shaped Holes," ASME Paper No. 97-GT-271.

[7] Brittingham, R.A. and Leylek, J.H., 1997, "A Detailed Analysis of Film Cooling Physics Part IV: Compound-Angle Injection with Shaped Holes," ASME Paper NO. 97-GT-272.

[8] Cho, H.H., Rhee, D.H., and Kim, B.G., 2001, "Enhancement of Film Cooling Performance Using a Shaped Film Cooling Hole with Compound Angle Injection," JSME International Journal, Series B, **44**, No. 1, pp. 99-110.

[9] Goldstein, R.J., Eckert, E.G., Eriksen, V.L., and Ramsey, J.W., 1970, "Film Cooling Following Injection Through Inclined Circular Tubes," Israel Journal of Technology, **8**, pp. 145-154.

[10] Jubran, B., and Brown, A., 1985, "Film Cooling From Two Rows of Holes Inclined in the Streamwise and Spanwise Directions," ASME J. Eng. Gas Turbines Power, **107**, pp. 84–91.

[11] Jabbari, M. Y., and Goldstein, R. J., 1978, "Adiabatic Wall Temperature and Heat Transfer Downstream of Injection Through Two Rows of Holes," ASME J. Eng. Power, **100**, pp. 303–307.

[12] Jubran, B. A., and Maiteh, B. Y., 1999, "Film Cooling and Heat Transfer From a Combination of Two Rows of Simple and/or Compound Angle Holes in Inline and/or Staggered Configurations," Int. J. of Heat and Mass Transfer, **34**, pp. 495–502.

[13] Ligrani, P. M., Wigle, J. M., Ciriello, S., and Jackson, S. M., 1994, ''Film Cooling From Holes With Compound Angle Orientations: Part1: Results Downstream of Two Staggered Rows of Holes With 3D Spanwise Spacing," Int. J. of Heat and Mass Transfer, **116**, pp. 341–352.

[14] Dittmar, J., Schulz, A., and Wittig, S., 2003, "Assessment of Various Film Cooling Configurations Including Shaped and Compound Angle Holes Based on Large-Scale Experiments," ASME J. Turbomachinery, **125**, pp. 57-64.

[15] Kim, Y.J., and Kim, S.M., 2003, "Influence of Shaped Injection Holes on Turbine Blade Leading Edge Film Cooling," Int. J. of Heat and Mass Transfer, **47**, pp. 245-256.

[16] Walters, D.K., and Leylek, J.H., 2000, "A Detailed Analysis of Film Cooling Physics. Part I: Streamwise Injection with Cylindrical Holes," ASME J. Turbomachinery. **122**, pp. 102–112.

[17] Saumweber, C., Schulz, A., and Wittig, S., 2003, "Free-Stream Turbulence Effects on Film Cooling With Shaped Holes," ASME J. Turbomachinery, **125**, pp. 65-73.

[18] Kadotani, K., and Goldstein, R. J., 1979, ''On the Nature of Jets Entering a Turbulent Flow Part A: Jet-Mainstream Interaction,'' ASME J. Eng. Power, **101**, pp. 459–465.

[19] Kadotani, K., and Goldstein, R. J., 1979, "On the Nature of Jets Entering a Turbulent Flow Part B: Film Cooling Performance," ASME J. Eng. Power, **101**, pp. 466–470.

[20] Jumper, G. W., Elrod, W. C., and Rivir, R. B., 1991, "Film Cooling Effectiveness in High Turbulence Flow,'' ASME J. Turbomachinery, **113**, pp. 479–483.

[21] Bons, J. P., MacArthur, C. D., and Rivir, R. B., 1996, "The Effect of High Free-Stream Turbulence on Film Cooling Effectiveness," ASME J. Turbomachinery, **118**, pp. 814–825.

[22] Burd, S. W., Kaszeta, R. W., and Simon, T. W., 1998, "Measurements in Film Cooling Flows: Hole L/D and Turbulence Intensity Effects,'' ASME J. Turbomachinery, **120**, pp. 791–797.

[23] Teng, S., Han, J. C., and Poinsatte, P. E., 2001, "Effect of Film-Hole Shape on Turbine Blade Heat Transfer Coefficient Distribution," J. of Thermophysics and Heat Transfer, **15**, pp. 249–256.

[24] Teng, S., Han, J. C., and Poinsatte, P. E., 2001, "Effect of Film-Hole Shape on Turbine Blade Film Cooling Performance," J. Thermophysics and Heat Transfer, **15**, pp. 257–265.

[25] Ou, S., Han, J.C., Mehendale, A.B., and Lee, C.P., 1994, "Unsteady Wake Over a Linear Turbine Blade Cascade with Air and CO2 Film Injection. Part I: Effect on Heat Transfer Coefficients." ASME J. Turbomachinery, **116**, pp. 721-729.

[26] Mehandale, A. B., Han, J. C., Ou, S., and Lee, C. P., 1994, "Unsteady Wake over a Linear Turbine Blade Cascade with Air and CO_2 Film Injection: Part II: Effect on Film Effectiveness and Heat Transfer Distributions," ASME J. Turbomachinery, **116**, pp. 730–737.

[27] Ekkad, S.V., Nasir, H., Acharya, S., 2000, "Film Cooling on a Flat Surface with a Single Row of Cylindrical Angled Holes: Effect of Discrete Tabs," Proceedings of 2000 IMECE, Orlando, Florida.

[28] Nasir, H., Sumanta, A., and Ekkad, S., 2003, "Improved Film Cooling From Cylindrical Angled Holes with Triangular Tabs: Effect of Tab Orientations," Int. J. of Heat and Fluid Flow, **24**, pp. 657-668.

[29] Hay, N., and Lampard, D., 1998, "Discharge Coefficient of Turbine Cooling Holes: A Review," ASME J. of Turbomachinery, **120**, pp. 314–319.

[30] Hay, N., Lampard, D., and Benmansour, S., 1983, "Effect of Crossflows on the Discharge Coefficient of Film Cooling Holes," ASME J. Eng. Power, **105**, pp. 243–248.

[31] Rowbury, D. A., Oldfield, M. L. G., and Lock, G. D., 1997, "Engine Representative Discharge Coefficients Measured in an Annular Nozzle Guide Vane Cascade," ASME Paper No. 97-GT-99.

[32] Gritsch, M., Saumweber, C., Schulz, A., Wittig, S., and Sharp, E., 2000, "Effect of Internal Coolant Cross-flow Orientation on the Discharge Coefficient of Shaped Film Cooling Holes," ASME J. Turbomachinery, **122**, pp. 146-152.

[33] Ekkad, S.V., and Han, J.C., 2000, "A Transient Liquid Crystal Thermography Technique for Gas Turbine Heat Transfer Measurements," Measurement Science Technology, **11**, pp. 957-968.

[34] Kwak, J.S., Han, J.C., 2003, "Heat Transfer Coefficients and Film Cooling Effectiveness on the Squealer Tip of a Gas Turbine Blade," ASME J. Turbomachinery, **125**, pp. 648-657.

[35] Zhang, L. and Jaiswal, R.S., 2001, "Turbine Nozzle Endwall Film Cooling Study Using Pressure Sensitve Paint," ASME J. Turbomachinery, **123**, pp. 730-738.

[36] Zhang, L.J. and Fox, M., 1999, "Flat Plate Film Cooling Measurements using PSP Gas Chromatograph Techniques," Proc. Fifth ASME/JSME Joint Thermal Engineering Conference, San Diego, CA.

[37] Mehendale, A.B., and Han, J.C., 1992, "Influence of High Mainstream Turbulence on Leading Edge Film Cooling Heat Transfer: Effect of Film Hole Spacing," Int. J. of Heat Mass Transfer, **35**, No. 10, pp. 2593-2604.

[38] Young, C.D., Han, J.C., Huang, Y., and Rivir, R.B., 1992, "Influence of Jet-Grid Turbulence on Flat Plate Turbulent Boundary Layer Flow and Heat Transfer," ASME J. Heat Transfer, **114**, pp. 65-72.

[39] Kline, S.J., and McClintock, F.A., 1953, "Describing Uncertainties in a Single Sample Experiment," Mechanical Engineering, **75**, pp. 3-8.

[40] Ligrani, P.M., Wigle, J.M., and Jackson, S.W., 1994, "Film Cooling From Holes with Compound Angle Orientation: Part 2: Results Downstream of a Single Row of Holes with 6D Spanwise Spacing," ASME J. Heat Transfer, **116**, pp. 353-362.

[41] Nasir, H., Ekkad, S.V., and Acharya, S., 2001, "Effect of Compound Angle Injection on a Flat Surface Film Cooling with Large Streamwise Injection Angle," Experimental Thermal and Fluid Science, **25**, pp. 23-29.

[42] Goldstein, R.J., and Jin, P., 2001, "Film Cooling Downstream of a Row of Discrete Holes with Compound Angle," ASME J. Turbomachinery, **123**, pp. 222-230.

[43] Jung, I.S., and Lee, J.S., 2000, "Effects of Orientation Angles on Film Cooling Over a Flat Plate: Boundary Layer Temperature Distributions and Adiabatic Film Cooling Effectiveness," ASME J. Turbomachinery, **122**, pp. 153-160.

VITA

Trent Alan Varvel is from Hearne, Texas, and received his Bachelor of Science degree in mechanical engineering from Texas A&M University in December, 2002. He will receive his Master of Science degree in mechanical engineering from Texas A&M University in December, 2004, while working under Dr. J.C. Han as a research assistant. He has worked for Siemens Westinghouse Power Incorporation during the summer of 2003 in their turbine heat transfer division. Trent's permanent address is as follows:

1203 Anderson
Hearne, TX, 77859
Email: tav4248@hotmail.com